AGU ADVANCING EARTH AND SPACE SCIENCE

JGR Planets

Key Points:
- The annual Martian O_3 distribution has been measured at a vertical resolution up to 0.2 km and for the first time alongside H_2O profiles
- O_3 and H_2O show strong vertical anti-correlation around aphelion as expected, contrasted with vertical correlation toward perihelion
- O_3 abundances between altitudes of 20–40 km are an order of magnitude higher at sunrise than at sunset between $L_S = 40°$–$50°$

Correspondence to:
M. R. Patel,
manish.patel@open.ac.uk

ExoMars TGO/NOMAD-UVIS Vertical Profiles of Ozone: 1. Seasonal Variation and Comparison to Water

M. R. Patel[1,2] ![ORCID], **G. Sellers[1]** ![ORCID], **J. P. Mason[1]** ![ORCID], **J. A. Holmes[1]** ![ORCID], **M. A. J. Brown[1]**, **S. R. Lewis[1]** ![ORCID], **K. Rajendran[1]**, **P. M. Streeter[1]** ![ORCID], **C. Marriner[1]**, **B. G. Hathi[1]**, **D. J. Slade[1]**, **M. R. Leese[1]**, **M. J. Wolff[3]** ![ORCID], **A. S. J. Khayat[4,5]** ![ORCID], **M. D. Smith[4]**, **S. Aoki[6,7]** ![ORCID], **A. Piccialli[6]** ![ORCID], **A. C. Vandaele[6]**, **S. Robert[6,8]** ![ORCID], **F. Daerden[6]** ![ORCID], **I. R. Thomas[6]** ![ORCID], **B. Ristic[6]** ![ORCID], **Y. Willame[6]**, **C. Depiesse[6]**, **G. Bellucci[9]**, and **J.-J. Lopez-Moreno[10]**

[1]School of Physical Sciences, The Open University, Milton Keynes, UK, [2]Space Science and Technology Department, Science and Technology Facilities Council, Rutherford Appleton Laboratory, Oxfordshire, UK, [3]Space Science Institute, Boulder, CO, USA, [4]NASA Goddard Space Flight Center, Greenbelt, MD, USA, [5]Center for Research and Exploration in Space Science and Technology II, University of Maryland, College Park, MD, USA, [6]Royal Belgian Institute for Space Aeronomy, BIRA-IASB, Brussels, Belgium, [7]LPAP, STAR Institute, Université de Liège, Liège, Belgium, [8]Institute of Condensed Matter and Nanosciences, Université catholique de Louvain, Louvain-la-Neuve, Belgium, [9]Istituto di Astrofisica e Planetologia Spaziali, IAPS-INAF, Rome, Italy, [10]Instituto de Astrofisica de Andalucia, IAA-CSIC, Glorieta de la Astronomia, Granada, Spain

Abstract We present ~1.5 Mars Years (MY) of ozone vertical profiles, covering $L_S = 163°$ in MY34 to $L_S = 320°$ in MY35, a period which includes the 2018 global dust storm. Since April 2018, the Ultraviolet and Visible Spectrometer channel of the Nadir and Occultation for Mars Discovery (NOMAD) instrument aboard the ExoMars Trace Gas Orbiter has observed the vertical, latitudinal and seasonal distributions of ozone. Around perihelion, the relative abundance of both ozone and water (from coincident NOMAD measurements) increases with decreasing altitude below ~40 km. Around aphelion, localized decreases in ozone abundance exist between 25 and 35 km coincident with the location of modeled peak water abundances. High-latitude (>±55°), high altitude (40–55 km) equinoctial ozone enhancements are observed in both hemispheres (L_S ~350°–40°) and discussed in the companion article to this work (Khayat et al., 2021). The descending branch of the main Hadley cell shapes the observed ozone distribution at $L_S = 40°$–$60°$, with the possible signature of a northern hemisphere thermally indirect cell identifiable from $L_S = 40°$–$80°$. Morning terminator observations show elevated ozone abundances with respect to evening observations, with average ozone abundances between 20 and 40 km an order of magnitude higher at sunrise compared to sunset, attributed to diurnal photochemical partitioning along the line of sight between ozone and O or fluctuations in water abundance. The ozone retrievals presented here provide the most complete global description of Mars ozone vertical distributions to date as a function of season and latitude.

Plain Language Summary We present over two years of new observations of the vertical distribution of ozone in the atmosphere of Mars. The ExoMars Trace Gas Orbiter spacecraft has been recording observations of the Martian atmosphere since 2018 to map the presence and changes in abundance of gases such as ozone by using the "Nadir and Occultation for Mars Discovery (NOMAD)" instrument. NOMAD continually observes the change in ozone abundance (among other gases) at different heights across much of the planet. These abundance profiles have revealed the presence of distinct layers of ozone enhancement at high altitudes in the atmosphere of Mars toward the polar regions and between spring and autumn in the southern hemisphere of Mars, discussed in detail in the companion article. We observe broad periods where often the abundance of ozone follows the abundance of water from ~10 km altitude up to ~50 km altitude, and other times when the two appear to be opposite in their variation with height. Our retrievals of ozone from NOMAD data provide the first coincident observations of ozone and water and provide previously unavailable information on the photochemistry of Mars.

Writing – review & editing: M. R. Patel

1. Introduction

Ozone (O_3) is a highly reactive trace gas in the Martian atmosphere, where odd-hydrogen (OH, HO_2, H, H_2O_2) catalytic products of water vapor photolysis dominate Mars photochemistry (McElroy & Donahue, 1972; Parkinson & Hunten, 1972), and contribute the primary loss mechanism for Mars O_3. As a consequence, large spatial and temporal changes in Mars O_3 were quickly recognized to be associated with condensation-driven variations in atmospheric water vapor (Barth et al., 1973; Clancy & Nair, 1996; Kong & McElroy, 1977; Shimazaki & Shimizu, 1979). Mars atmospheric water variations result from seasonal/spatial variations in loss or supply to seasonal and residual polar ice caps (Fedorova et al., 2006; Jakosky & Farmer, 1982; Khayat et al., 2019; Pankine & Tamppari, 2019; Smith, 2004; Smith et al., 2009; Steel et al., 2014); and by the large spatial/temporal variations in ice cloud saturation conditions in the Mars atmosphere (Clancy et al., 1996; Montmessin et al., 2004; Navarro et al., 2014; Neary et al., 2020).

Mariner 7 made the first detection of O_3 in the Martian atmosphere (Barth & Hord, 1971) and later Mariner 9 showed O_3 to be seasonally variable (Barth et al., 1973). Subsequent missions and ground-based observations have characterized the geographical and seasonal variability of O_3 extensively (e.g., Blamont & Chassefière, 1993; Clancy et al., 1999, 2016; Fast et al., 2006; Lebonnois et al., 2006; Lefèvre & Krasnopolsky, 2017; Lefèvre et al., 2021; Montmessin & Lefèvre, 2013; Perrier et al., 2006). This has led to the well-established O_3 climatology of increased column abundances in the cold, dry atmospheric conditions of the fall and winter high-latitude regions; and reduced substantially in abundance over warmer, wetter low latitude and summer high-latitude regions. In addition, a distinct-low latitude, mid-altitude peak in O_3 arises from ~20 K colder atmospheric (and surface) temperatures present around Mars aphelion (Clancy & Nair, 1996), when Mars is furthest from the Sun in its eccentric orbit (at the current epoch, this occurs around Mars northern summer at a solar longitude, L_S, of 71°). These basic temporal and spatial behaviors of Mars atmospheric O_3 and H_2O column abundances are qualitatively reproduced in Mars global circulation models (GCM; e.g., Daerden et al., 2019; Holmes et al., 2017, 2020, 2018; Lefèvre et al., 2008, 2004).

However, most of the above behaviors are primarily characterized in terms of column O_3 measurements, due to the limited extent of vertical profile measurements for O_3 (Clancy et al., 2017; Gröller et al., 2018; Lebonnois et al., 2006; Olsen et al., 2020; Piccialli et al., 2021) or H_2O (Fedorova et al., 2018; Maltagliati et al., 2013). This is a significant limitation given the importance of vertical profile dependences in characterizing these photochemical and water vapor saturation (cloud microphysical) processes in any detail. Surprisingly, our understanding of such a fundamental relationship as the anti-correlation of Mars atmospheric O_3 and H_2O is obscured by uncertainties associated with column O_3 and H_2O measurement comparisons. Current model-data comparisons for these column data sets have implied significant (50%–100%) excesses in observed atmospheric O_3, while reproducing observed water column abundances more closely (Lefèvre et al., 2008). Heterogenous reduction of HO_x on Mars water ice clouds has been proposed to account for such elevated O_3 abundances relative to homogeneous (gas-phase only) photochemical predictions (Lefèvre et al., 2008). Subsequent Mars O_3 observations have not yet indicated a heterogenous solution but the model underestimations of O_3 columns remain unresolved (Clancy et al., 2016; Daerden et al., 2019). It is possible, perhaps likely, that inaccurate model simulations of water vapor (and O_3) profiles contribute significantly to this issue (Clancy et al., 2017). Column O_3 measurements are heavily weighted by O_3 abundances in the lower scale height (~10 km), a region untouched by profile measurements to date. Column H_2O measurements do not provide significant guidance to temperature-sensitive, process-complicated simulations of cloud microphysics, necessary to simulate water vapor profiles accurately (e.g., Navarro et al., 2014).

Consequently, ExoMars Trace Gas Orbiter (TGO) sensitive and accurate determinations for O_3 profiles through UV (260 nm Hartley band) solar occultations (SOs) (this article), and water vapor profiles through near-IR SOs (NOMAD- Aoki et al., 2019, Vandaele et al., 2019; ACS- Fedorova et al., 2020), represent a major observational advance in the study of Mars photochemistry. On their own, Nadir and Occultation for Mars Discovery (NOMAD) O_3 profile retrievals yield a unique vertical dimension to our definition of Mars photochemistry. Coincident with NOMAD water profile retrievals, they enable an intrinsically diagnostic study of Mars O_x (O + O_3) and HO_x chemistry. Remaining contradictions on the presence of atmospheric methane (Korablev et al., 2019) and recent ExoMars detections of atmospheric HCl (Aoki et al., 2019; Korablev et al., 2021) lead to renewed importance in establishing a detailed understanding of Mars photochemistry.

Here, we present retrieved NOMAD O_3 profiles, with an emphasis on generating a global view of Mars photochemistry (O_3) in the vertical dimension. Preliminary comparisons of these NOMAD O_3 profile retrievals are provided with published NOMAD water profile retrievals (over L_S = 163°–345° in MY34, Aoki et al., 2019) and modeled water profiles (Holmes et al., 2020) extending over the remaining L_S range of presented O_3 profiles. An initial comparison of modeled O_3 profiles indicates the degree to which existing models, without assimilated NOMAD water profile retrievals, correspond to the NOMAD O_3 profile measurements. Following studies of the combined NOMAD water and O_3 profile data sets will employ data assimilation of NOMAD water profile measurements to fully realize anticipated advances in Mars photochemistry associated with NOMAD O_3 and H_2O profile data.

Vertical profile measurements by the NOMAD spectrometer suite, aboard the ESA/Roscosmos ExoMars TGO mission have now been taken for over 1.5 Mars Years (MY), allowing the first glimpse into the vertical distribution of O_3 in the atmosphere of Mars. In this article, we present O_3 vertical profiles from April 2018 to November 2020, covering over 1.5 MY of O_3 measurements. This period includes the MY34 global dust storm, as well as the occurrence of a regional storm (Guzewich et al., 2019). The companion article to this study (Khayat et al., 2021) studies the high-altitude enhancement observed in more detail. The details of the NOMAD observations and the retrievals method are described in Sections 2 and 3 respectively, and the observational results are discussed in Section 4.

2. Observations

2.1. ExoMars and NOMAD-UVIS

The Ultraviolet and Visible Spectrometer (UVIS) is one of three channels that comprise the NOMAD spectrometer suite, aboard ExoMars TGO. The other two channels of NOMAD are infrared (IR) spectrometers: the SO channel and the Limb Nadir and Occultation (LNO) channel. A full description of the SO and LNO channels can be found in Vandaele et al. (2015). UVIS covers the spectral range of 200–650 nm with a spectral resolution of <2 nm and is capable of (mutually exclusive) observations in both SO and nadir viewing geometries using a single spectrometer with the aim to provide a comprehensive understanding of the climatology and vertical distribution of ozone, dust aerosols and ice aerosols in the Martian atmosphere. At the time of writing, the UVIS nadir ozone retrievals are not yet published. The occultation channel provides the capability to not only measure these species in the vertical and spatial dimension but to also measure changes on seasonal and diurnal timescales. A full description of the NOMAD-UVIS channel can be found in Patel et al. (2017)

TGO is in a near-circular 74° inclined orbit with a periapsis of 380 km and apoapsis of 420 km and an orbital period of approximately 2 h. NOMAD occultations come in four flavors: two different pointing modes and two different spacecraft maneuvers. When the β-angle, the angle between the orbital plane and the direction to the Sun, is <20° TGO will actively track the Sun during an occultation, keeping the instrument boresight fixed on the Sun center. Within each planning period (approximately 1 month) around two of these sun-tracking occultations will be led using the UVIS boresight (i.e., the UVIS boresight is held centered on the Sun center); the rest are led by the NOMAD SO IR channel. At β-angles >20°, spacecraft angular momentum constraints prohibit suntracking and TGO rotates around the instrument pointing vector. This has minimal effect on UVIS-led occultations, however, on SO-led occultations, the UVIS occultation boresight (2 arcmin field of view) traces an arc around the solar disc at a distance from the solar center of approximately 0.3 solar radii. In general, there is no discernible impact on the calculated transmissions, since the UVIS boresight remains at the same radial distance from the center of the Sun, and the top of atmosphere reference transmission is defined over a range of altitudes using a linear regression method (see Section 2.3).

2.2. Data Set

Data acquired by the UVIS spectrometer from the start of the TGO science phase in April 2018 to November 2020 were used in this study, covering a period of just over one full Martian year (MY 34, L_S = 163° to MY 35, L_S = 320°). This data set comprises 5,990 solar occultations (3,051 egresses, 2,939 ingresses) and corresponds to the Level 1.0 data made available through the NOMAD PI institute. The derived retrieval data data set can be accessed freely through the Open Research Data Online repository (Patel, 2021).
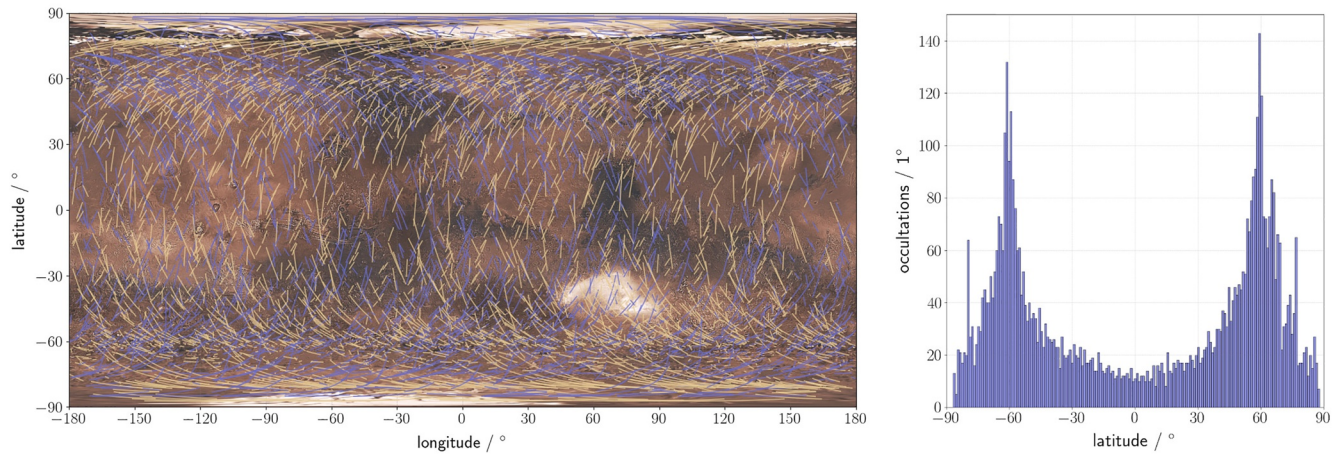
Figure 1. (left) Geographical coverage of UVIS occultation profiles represented as tangent point projected onto the Martian surface, for egress occultations (yellow) and ingress occultations (blue). (right) Histogram of the latitude of all occultations taken to date (latitude defined as the mid-point of the total occultation ground-track).

The geographical distribution of the occultation measurements is shown Figure 1. Due to TGO's orbital characteristics and the terminator geometry for SOs, the majority of occultations are to be found clustered symmetrically around ±63° latitude bands (Figure 1) in the northern and southern hemispheres, with minimally slanted (vertical) atmospheric profiles. Relatively few occultations penetrate the equatorial latitudes; those that do tend to exhibit very long ground tracks reflecting a highly slanted atmospheric profile.

The latitudinal progression of the occultations over the duration of the current data set is shown in Figure 2 and is controlled by the changing β-angle of the spacecraft orbit. The β-angle varies in a cyclic pattern, moving between low and high β-angle phases. At low β-angles an orbit will typically consist of both an ingress and egress occultation, alternating between high-latitudes in the northern and southern hemispheres. As the β-angle increases, the occultations tend toward equatorial latitudes until the orbital geometry (β-angles >60°) prohibits occultation pointing and results in a period of no occultation observations.

Each occultation occurs over a period of between approximately 1–7 min, with equatorial occultations generally having longer durations as a result of the longer slant paths. The total integration time of each measurement was 45 or 75 ms. In the initial phase of the science mission (L_S = 163°–345°), the UVIS sampling frequency was set to 3 s providing a spectral resolution of <2 nm. Since the altitude resolution is also dependent on the occultation duration, the 3 s sampling frequency initially gave vertical resolutions that varied between 0.7 and 4.4 km. This somewhat coarse altitude resolution for occultations with short durations was a result of the 3 s measurement rhythm which is set by the CCD readout time and the data transfer time from UVIS to the NOMAD data processing unit. The CCD read time is fixed and cannot be changed but the data transfer time can be reduced by sending less data. After L_S = 345°, UVIS was modified
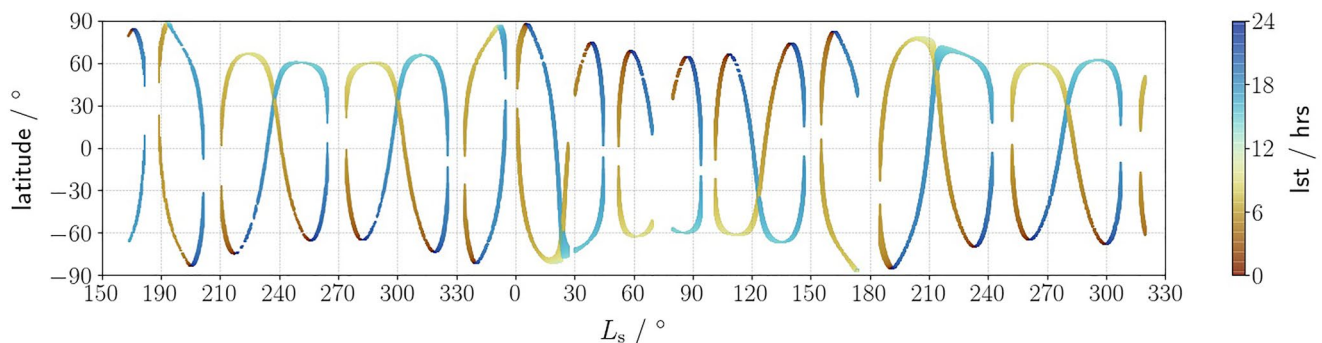

Figure 2. Latitude and local solar time variation of UVIS occultation measurements over time in solar longitude L_S.

to spectrally bin the CCD array from 1,024 pixels to 128 pixels, a factor of eight reduction in the data volume, allowing an increase in the sampling frequency to 1 s, a factor of three improvement, and a corresponding increase to the altitude resolution in the range 0.2–1.4 km. The spectral features of ozone, water ice aerosols, and dust aerosols are all broad band features, as such an increase in the spectral resolution to 4 nm had no impact on the retrievals.

A great benefit of the SO technique is that it does not rely on laboratory radiometric calibration, and it is a self-calibrating measurement. During a SO, the line of sight (LoS) between the instrument and the Sun is maintained as the LoS passes through the atmosphere, from a very high altitude (200–250 km) down to the surface (or vice versa). Relative transmission is then calculated using a reference spectrum obtained from high up in the atmosphere where no atmospheric contribution is expected (typically ~110 km), resulting in a consistently self-calibrated transmission profile through the atmosphere for each occultation. Additionally, no correction for UV airglow is required, given the significantly higher signal intensity from the line-of-sight Sun illumination with respect to atmospheric emission at these wavelengths.

2.3. Atmospheric Transmittance

This transmission is defined as the spectral radiance observed through the atmosphere at a given tangent altitude, z, above the surface, $S(\lambda, z)$, taken as a proportion of the total (above atmosphere) solar radiance, $S_0(\lambda)$:

$$T(\lambda, z) = \frac{S(\lambda, z)}{S_0(\lambda)} \tag{1}$$

$S_0(\lambda)$ is determined using the algorithm defined by Trompet et al. (2016), as discussed in Vandaele et al. (2018) as the standard occultation procedure for NOMAD transmissions. This method uses an iterative algorithm to define a mean value for spectra above 120 km, where it is assumed there is no absorption due to Martian atmospheric gases, thus defining a unique reference for each occultation.

The spectral transmission obtained from the data can be related to the number density of all-absorbing agents in the LoS through the atmosphere through the Beer-Lambert law:

$$S(\lambda, z) = S_0(\lambda) e^{-\Sigma_i \sigma_i N_i(z)} \tag{2}$$

where, σ_i is the cross-section of the ith absorbing chemical species and $N_i = \int n_i . dx$ is the integrated total number density per species along the LoS column. Given the small field of view, the signal contribution from forward scattering was modeled to be approximately two orders of magnitude lower than the direct solar signal and is considered negligible. A single transmission spectrum yields a transmission ratio for each wavelength in the detector range of 200–650 nm at a spectral resolution varying between approximately 1.5–3.5 nm (depending on observation configuration). An example of the corresponding set of transmission spectra obtained during a single occultation is shown in Figure 3, representing the observed transmission through different layers of the Martian atmosphere.

3. Retrieval Method

3.1. Spectral Inversion

The transmission spectra observed by the instrument at successive tangent altitudes above the surface are converted into number densities of different species by a spectral inversion process. These number density profiles, or slant densities, are a measure of the total integrated number of a given species in the line-of-sight column of each observation.
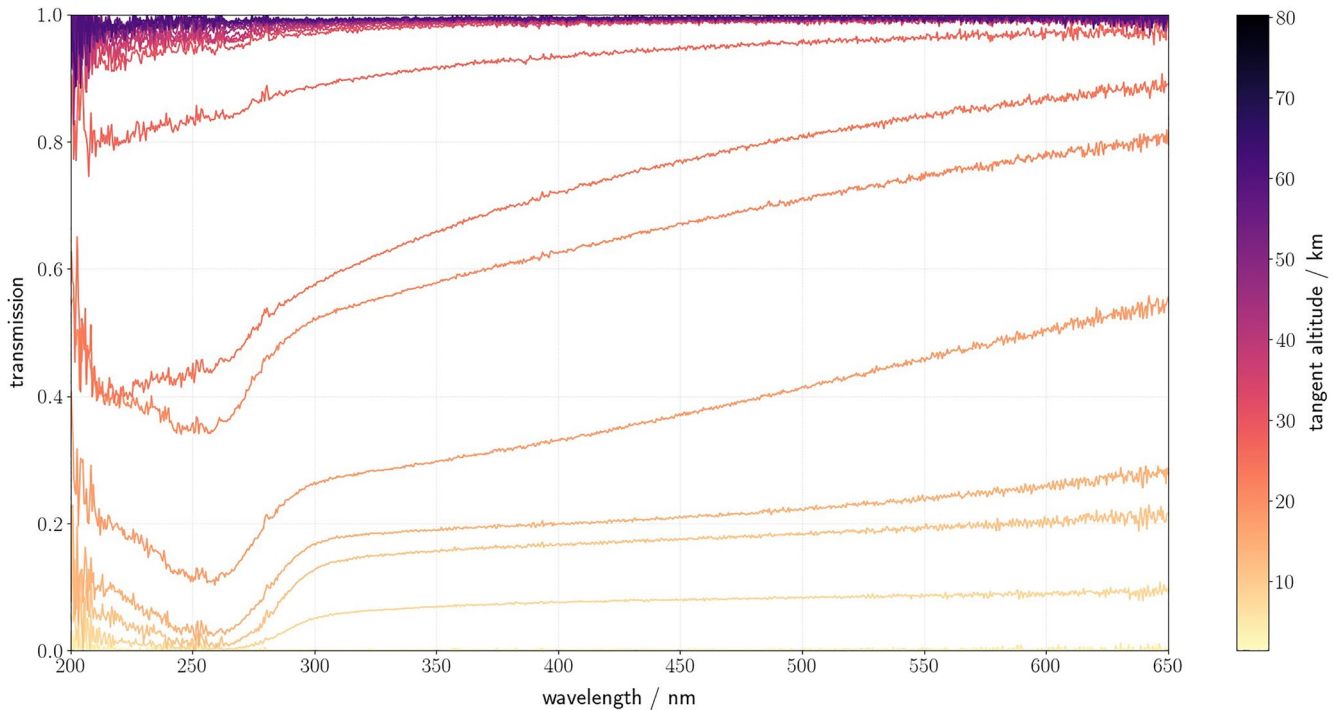
Figure 3. Transmission spectra at different tangent altitudes for an example UVIS occultation. Transmission values below 1% are not considered in the retrieval process.

3.1.1. The Line-of-Sight Points

A schematic of the location of the LoS between the TGO spacecraft and the Sun for each observation is shown in Figure 4. The tangent height point, denoted by $\mathbf{X}_{tan}$, is defined as the point along the LoS that has the shortest distance from the LoS to the center of the planet.

The geometry parameters recorded in each observation specify the height of TGO above the center of the planet R_{sat}, together with the planetocentric latitude θ_{sat} and longitude ϕ_{sat} of the TGO position. They also give the height H_{tan} of the tangent point above the MGM1025 areoid (Lemoine et al., 2001), defining the term "altitude" used throughout this article.

It is useful to define a cartesian coordinate system with origin at the center of the planet, the positive x axis cutting the 0° meridian, and the positive z axis passing through the north pole. Then, using the geometry of the ellipsoid, it is possible to calculate the cartesian coordinates $\mathbf{x}_{sat} = \left[x_{sat}, y_{sat}, z_{sat} \right]$ of the point on the
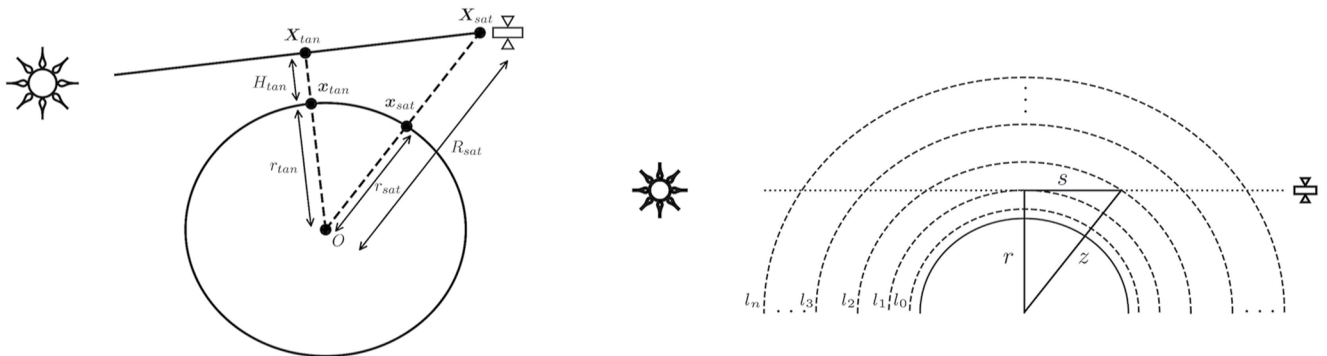
Figure 4. (left) Geometry of an occultation observation. (right) The geometry of the inversion procedure with observationally defined atmospheric layers, l_n. r is the distance from the center of Mars to the tangent point of the LoS, z is the distance from the center of Mars to each successive layer and z is half the path length through that and all internal layers.

ellipsoid corresponding to the position $(\theta_{sat}, \phi_{sat})$. This is done by first calculating the corresponding radial distance r_{sat} of the point from the center of the ellipsoid:

$$
\begin{aligned}
r_{sat} &= \sqrt{\left[\left(\frac{\cos(\theta_{sat})}{a}\right)^2 + \left(\frac{\sin(\theta_{sat})}{c}\right)^2\right]^{-1}}, \\
x_{sat} &= r_{sat}\cos(\theta_{sat})\cos(\phi_{sat}), \\
y_{sat} &= r_{sat}\cos\theta_{sat}\sin\phi_{sat}, \\
z_{sat} &= r_{sat}\sin\theta_{sat}.
\end{aligned}
\tag{3}
$$

Since $\mathbf{x}_{sat}$ is collinear with the center of the planet and the location of the satellite $\mathbf{X}_{sat}$, a simple rescaling then gives the cartesian coordinates of the satellite location:

$$
\mathbf{X}_{sat} = \frac{R_{sat}}{r_{sat}}\mathbf{x}_{sat}.
\tag{4}
$$

Similarly, it is possible to calculate the cartesian coordinates $\mathbf{X}_{tan}$ of the tangent height point, by rescaling the cartesian coordinates of the point $\mathbf{x}_{tan}$ on the ellipsoid corresponding to the position $(\theta_{tan}, \phi_{tan})$. The procedure is as described above for the case of $\mathbf{X}_{sat}$, except that the final rescaling is given as follows:

$$
\mathbf{X}_{tan} = \frac{r_{tan} + H_{tan}}{r_{tan}}\mathbf{x}_{tan}.
\tag{5}
$$

Once the cartesian coordinates of $\mathbf{X}_{sat}$ and $\mathbf{X}_{tan}$ are known, the LoS points are readily calculated as points that lie along the line joining $\mathbf{X}_{sat}$ and $\mathbf{X}_{tan}$. It is noted that the effect of refraction in low-pressure atmospheres has been found to be small by previous studies (e.g., Bellucci et al., 2009; Bétrémieux & Kaltenegger, 2015; Hubbard et al., 2001) and therefore refraction effects are not considered here.

3.1.2. GCM and Re-Analysis

To perform the spectral fitting (described in the next section), initial estimates of aerosol opacity and ozone abundance along the LoS points are determined. These initial estimates are not strictly needed to perform the initial opacity retrieval, but are used for subsequent mixing ratio calculations, and were therefore used as initial estimates to optimize the fitting process since they were available. These values were extracted from outputs of the Open University (OU) modeling group Mars GCM coupled to the Analysis Correction assimilation scheme that has a strong heritage in data assimilation on Mars (Holmes et al., 2020, 2018, 2019; Lewis et al., 2007; Montabone et al., 2006, 2014; Streeter et al., 2020). The GCM is comprised of physical parameterisations (Forget et al., 1999) and a photochemical module (Lefèvre et al., 2008, 2004) shared with the Laboratoire de Météorologie Dynamique (LMD) modeling group, alongside a spectral dynamical core and semi-Lagrangian advection scheme (Newman et al., 2002). It includes the latest sub-models to provide the most realistic modeling of the turbulent processes in the planetary boundary layer (Colaïtis et al., 2013), and a water-ice cloud microphysics package (Navarro et al., 2014) that includes radiatively active water ice clouds and supersaturation. The OU modeling group GCM has been developed in a collaboration between the OU, the LMD, the University of Oxford, and the Instituto de Astrofisica de Andalucia. Initial O_3 values originate from a model run that assimilated O_3 column data measured by the SPICAM instrument during MY 27 (Holmes et al., 2018). Although this model run is for a different year, it produces a good initial estimate of ozone for the beginning of the model run assuming that the seasonal O_3 distribution is repeatable from year to year. For temperature, dust and aerosol fields, a different model run was used, that assimilated contemporaneous temperature profiles and column dust data measured by the Mars Climate Sounder (MCS) instrument (Streeter et al., 2020). The basis of the dust distribution for this period is presented in Montabone et al. (2020).

3.1.3. Cross-Sections

The three primary absorption features acting on the observed atmospheric transmissions in the observational wavelength region between 200 and 650 nm are those due to carbon dioxide (CO_2), aerosols, and O_3. Only the cross-section of O_3 is of relevance in this study since wavelengths close to CO_2 absorption are

not considered, and the O_3 cross-section values at 218 K of Malicet et al. (1995) are used here. The spectral absorption characteristics of aerosols exhibit a continuum attenuation in the transmission spectra so an increase in aerosol abundance can in principle be modeled as a fit to any part of the spectra well separated from the reserved O_3 band. Due to the spectral shape changes at longer wavelengths due to aerosol particle size these wavelengths are avoided for modeling the aerosol content in the spectra.

3.1.4. Spectral Fitting

A least squares (χ^2) procedure involving minimizing the sum of the squares of the residual differences between the measured transmissions and the best fit model across a range of wavelengths, is performed utilizing the Levenberg-Marquardt algorithm to obtain the best fit solution. Modeled values for aerosol opacity and ozone abundance are extracted for each LoS from the assimilated data set described earlier as *a priori* values for the iterative fitting process, purely to reduce the number of iterations required.

The first iteration of the fitting is performed in the region between 320 and 360 nm (i.e., outside the O_3 absorption band) for the aerosol abundance determination (Clancy et al., 2016), with an optional additional region at 220–230 nm to adjust for CO_2 Rayleigh scattering (Ityaksov et al., 2008) across the O_3 band when required. Due to the reduced performance of the detector in this shorter wavelength fit region, in instances when the measured transmission in this region results in negative retrieved values of CO_2 Rayleigh scattering, an aerosol re-fit constrained solely to the 320–360 nm region is performed around the initial obtained aerosol value and the re-fitted aerosol fit is extrapolated over the O_3 band. All parameters in the model were initially fixed except for the CO_2 Rayleigh scattering contribution and aerosol abundances along with the Angstrom coefficient, which were treated as free parameters over each iteration to determine an aerosol abundance, after CO_2 Rayleigh scattering, on convergence. The fitting procedure for O_3 abundance then follows, with updated CO_2 Rayleigh scattering and aerosol values fixed in the model, within the wavelength range 240–320 nm on the positive gradient of the O_3 Hartley band. This wavelength range was used since it permits an accurate representation of O_3 abundance based on a measure of the depth of this feature in the spectrum, whilst avoiding the CO_2 Rayleigh scattering fit region and the less well-characterized transmission values below 220 nm, where there is greater noise in the spectra and straylight contamination represented by a growth in relative errors.

This optimal wavelength range over which to perform the O_3 fit coincides with the magnesium II h and k doublet solar emission at 280 nm, which is often used as a diagnostic of solar activity (e.g., Snow et al., 2019). As the determination of the Hartley band depth in any given spectrum may be influenced by the residual presence of this feature as the LoS moves across the solar disk, the values at 280 nm are discarded and an interpolation is performed either side of this wavelength.

Examples of the fitting procedure results on two example occultations are shown in Figure 5 where the overall composite fit has been combined to construct the final modeled transmission. The O_3 model sometimes deviates from the observation below 255 nm primarily due to known straylight within the system causing a non-real excess in the recorded transmission values below this threshold. In general, the results <220 nm are not considered here due to the loss in responsivity of the CCD at these wavelengths (Patel et al., 2017). A lower altitude cut-off is applied to all profiles at the 1% transmission level at a wavelength of 255 nm, below which the signal on the CCD detector becomes comparable to the noise. Using the total abundance extracted from the O_3 fit of the modeled spectra coupled with the cross-section values the total integrated number density (slant density) is then calculated by applying the Beer-Lambert law defined in Section 2.3.

3.2. Vertical Inversion

The slant density of an absorbing species gives a measure of the total integrated number of molecules per unit area along the LoS of each measurement. To convert this slant density profile into an associated set of local densities, or a true vertical profile, a vertical inversion of the slant densities is performed.

To achieve this inversion a standard onion peeling process is used (Auvinen et al., 2002; Quémerais et al., 2006; Rodgers, 2000), a procedure that requires the observed two-dimensional atmospheric slice to be split into concentric layers. This structure, illustrated in Figure 4, is provided by the observational data, each layer being defined by the tangent altitude of the LoS in successive measurements above the same areoid
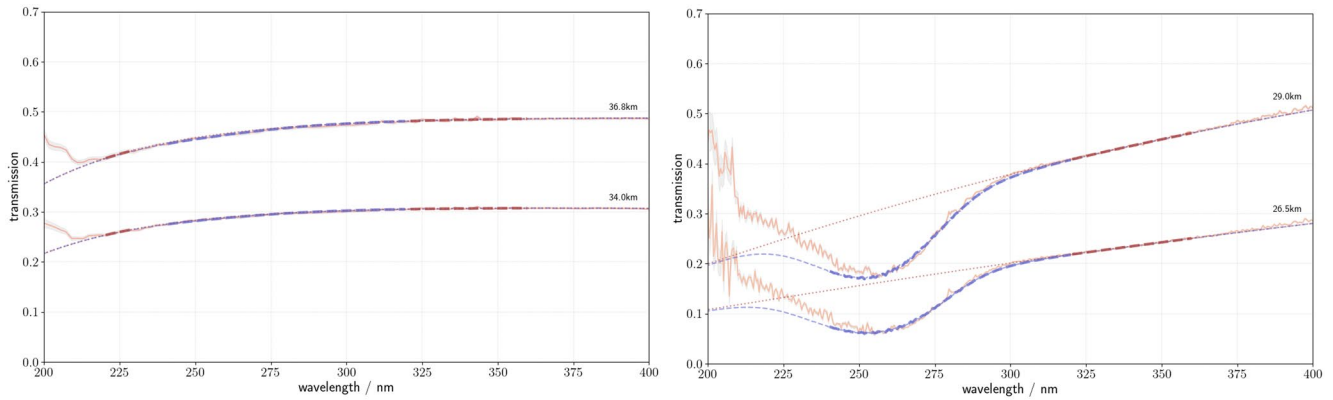
Figure 5. Transmission spectra for two altitudes in two examples of occultations with and without ozone present. (left) Occultation 20180621_195637 (latitude = 49.3°N, Longitude = 86.7°, L_S = 197°), with aerosol fit between 320–360 nm and 220–230 nm to adjust for CO_2 Rayleigh scattering characterization (thick dashed red), extrapolation (dotted red), subsequent 240–320 nm O_3 fit (thick dashed purple) to the observed transmission and associated uncertainty (gray region) with the final modeled transmission (thin dashed purple), showing no observed ozone. (right) Occultation 20180503_012553 (latitude = 75.1°N, Longitude = −86.9°, L_S = 169°) with only the 320–360 nm aerosol fit extrapolated and subsequent O_3 fit performed in the same manner, showing a clear identification of O_3. Note that the 220–230 nm fitting region is also shown in this plot, but it is not used in the fitting process due to the poor data quality at these wavelengths in this occultation.

surface defined in Section 3.1. This results in a single measured transmission spectrum corresponding to each atmospheric layer. A spherically symmetric atmosphere is assumed in the plane defined by the observed lines of sight. It should be noted that O_3 is unlikely to be distributed in a spherically symmetric manner along the line of sight along the terminator (see e.g., Piccialli et al., 2021 for a discussion of this issue), and therefore this assumption will have some associated (unavoidable) error, that cannot be quantified in a meaningful way at this time. The separate path lengths that every measurement's LoS takes through each of the atmospheric layers are then calculated geometrically:

$$S = \sqrt{z^2 - r_i^2} \qquad (6)$$

In combination with an interpolation between the layers, an Abel integral provides the coefficients of the individual elements of the weighting function matrix, **A**, which defines all combinations of path lengths per layer in the two-dimensional observational grid:

$$A_{ij} = \int_{z_{min,j}}^{z_{max,j}} f(z) \frac{z}{\sqrt{z^2 - r_i^2}} dz \qquad (7)$$

where $f(z)$ is the interpolated pressure as a function of altitude z, $z_{min,j}$ and $z_{max,j}$ are the altitude limits covered by the jth layer. All (virtual) path lengths constructed via this method that are external to the atmosphere will not contribute to the total observed abundance in any given atmospheric line-of-sight and therefore are given a zero weighting in the final matrix.

With the weighted path lengths encoded in the matrix **A** the local densities, **D**, forming the vertical profile can be calculated from the known slant densities, **N**, and their associated uncertainties, ϵ, by a matrix inversion of the form:

$$\mathbf{D} = \mathbf{N} \cdot \mathbf{A}^{-1} + \epsilon \qquad (8)$$

This then provides a final vertical profile from the observed slant densities. An example of a calculated O_3 vertical profile obtained through this method and its associated slant density profile are shown in Figure 6. Measured O_3 number densities range from ~10^{10} in the lower altitudes down to ~10^7 below which the noise floor inherent in the retrieved slant densities is reached, demonstrated here by the shaded envelope in Figure 6. Since in the present study only upper limits can be defined above ~60 km, the results presented here will focus on the detections confirmed below this altitude.
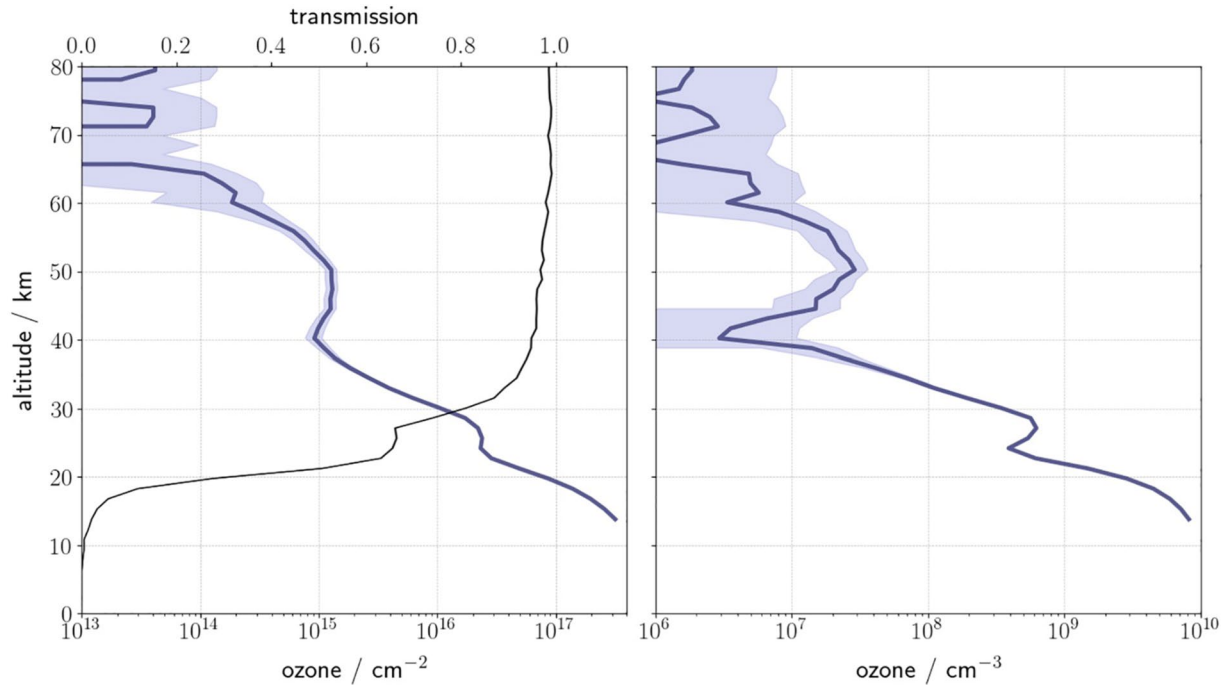
Figure 6. (left) O_3 slant number density (blue) and atmospheric transmission (black). (right) Subsequent derived O_3 vertical profile showing the variation in abundance between 80 and ~15 km. The increasing uncertainty above ~60 km is shown by the shaded envelope. This profile corresponds to observation file 20190808_142654, at $L_S = 63°$ in MY35 and a latitude of 62°S.

3.2.1. Uncertainties on the Vertical Profile

The main source of uncertainty in the occultation data arises from instrumental noise—each spectrum has an associated instrumental error value, with the median value of this error within each occultation being less than 1%.

To determine the associated uncertainty in the retrieval, the $1-\sigma$ experimental uncertainty from the random instrumental noise associated with every observed transmission, ϵ, is used in order to calculate a weighted deviation (W) between the model, as evaluated from the Beer-Lambert equation (Section 2.3), the fitted model data $M(\lambda)$, and the observation data $\mathbf{x}(\lambda)$:

$$W = \frac{M(\lambda) - \mathbf{x}(\lambda)}{\epsilon} \tag{9}$$

The square of these weighted residuals are the χ^2 values that, through successive iterations, are minimized in order to arrive at a final best fit solution to the modeled data, the associated cost function can be expressed as:

$$V = \mathbf{A}^T \mathbf{C}^{-1} \mathbf{A} \tag{10}$$

The covariance matrix, $\mathbf{C}$, in this process describes the covariance of every combination of pairs of measurements, the diagonal elements, therefore, represent the self-covariance (the variance) of each observation with itself, the individual errors on the obtained slant density measurements are thus obtained from the square-root of the diagonal of the covariance matrix. An averaging kernel, $\mathbf{K}$, is constructed from the weighting function and covariance matrices, whose ith row describes the weighting influence of each atmospheric layer on the ith LoS derived number density:

$$\mathbf{K} = \left(V + \lambda_s \mathbf{L}^T \mathbf{L}\right)^{-1} \left(\mathbf{A}^T \mathbf{C}^{-1}\right) \tag{11}$$

where the matrix $\mathbf{L}$, whose contribution is governed by the smoothness coefficient λ_s, is given by:

$$L = \frac{1}{h^2}\begin{bmatrix} -1 & 1 & 0 & 0 & \cdots & 0 \\ 1 & -2 & 1 & 0 & \cdots & 0 \\ 0 & 1 & -2 & 1 & \cdots & 0 \\ \vdots & \vdots & \vdots & \vdots & \ddots & \vdots \\ 0 & \cdots & 0 & 1 & -2 & 1 \\ 0 & \cdots & 0 & 0 & 1 & -1 \end{bmatrix} \tag{12}$$

This kernel represents the quality of the retrieval per retrieved number density value in the final vertical profile.

The uncertainty in the number densities of the final vertical profile is derived in an analogous way to the number densities themselves, as shown below. In an iterative procedure, the respective errors of each observed slant density are combined in quadrature with the sum of the previously calculated errors on all higher layers, weighted by the proportional path length that those layers represent in the current line of sight column:

$$\partial n_i = \sqrt{\frac{\left(\frac{\delta F_i}{2}\right)^2 + \sum_{j=0}^{i-1}\left[\delta n_j^2 \cdot dx_j^2\right]}{dx_i^2}} \tag{13}$$

This quantity is then scaled based on the path length of the layer in question (the lowest layer) in the current column to obtain a final error on the number density in that layer of the vertical profile. Median errors on the calculated number density are found to be up to 7% between an altitude range of 20–50 km.

4. Results and Discussion

4.1. O_3 Vertical Distribution

Figure 7 shows the seasonal variation of the O_3 vertical profiles from the NOMAD-UVIS retrievals for observations made in the northern hemisphere and the southern hemisphere. Generally, retrieved NOMAD O_3 profiles extend to 50–70 km altitudes, based on NOMAD O_3 sensitivity limits and Mars upper-level O_3 abundances (previous section, e.g., Figure 6). It should also be noted that these plots show the vertical profile over varying latitudes—in some cases, moving from the polar regions to equator in a small L_S period. Thus, care must be taken in interpreting these plots, as latitudinal gradients can appear mapped into temporal (L_S) changes.

Given the strong photochemical anticorrelation of O_3 with H_2O, we also present the water profiles simultaneously retrieved with the IR channel of NOMAD (Aoki et al., 2019), providing the first direct comparison of contemporaneous and co-located O_3 and H_2O vertical profiles. Unfortunately, at the time of writing NOMAD water profiles retrievals are only publicly available up to $L_S = 345°$ in MY34 (February 2019), and therefore the water profiles shown in Figure 7 only contain NOMAD water retrievals to $L_S = 345°$.

To provide a comparative water vapor data set for the remaining period through to $L_S = 320°$ in MY35 (November 2020), we performed an assimilation of MCS v5.3.2 temperature profiles and column dust retrievals (Kleinböhl et al., 2017) using the OU modeling group Mars GCM described in Section 3.1.1. An ensemble of assimilation runs was conducted over the whole time period, in which the parameters of albedo and thermal inertia of perennial surface ice were varied to select an optimum water vapor simulation. Navarro et al. (2014) adopted this approach in a forward GCM study, to model Mars atmospheric water column variations. The selected assimilation run was chosen to optimize water vapor comparisons with respect to NOMAD water vapor retrievals toward the end of the period for which they are available (late 2018, when the MY34 dust storm effects have largely abated). Comparison with as yet unpublished NOMAD water profile observations for this period show the modeled water to be qualitatively consistent with the observed water profiles.
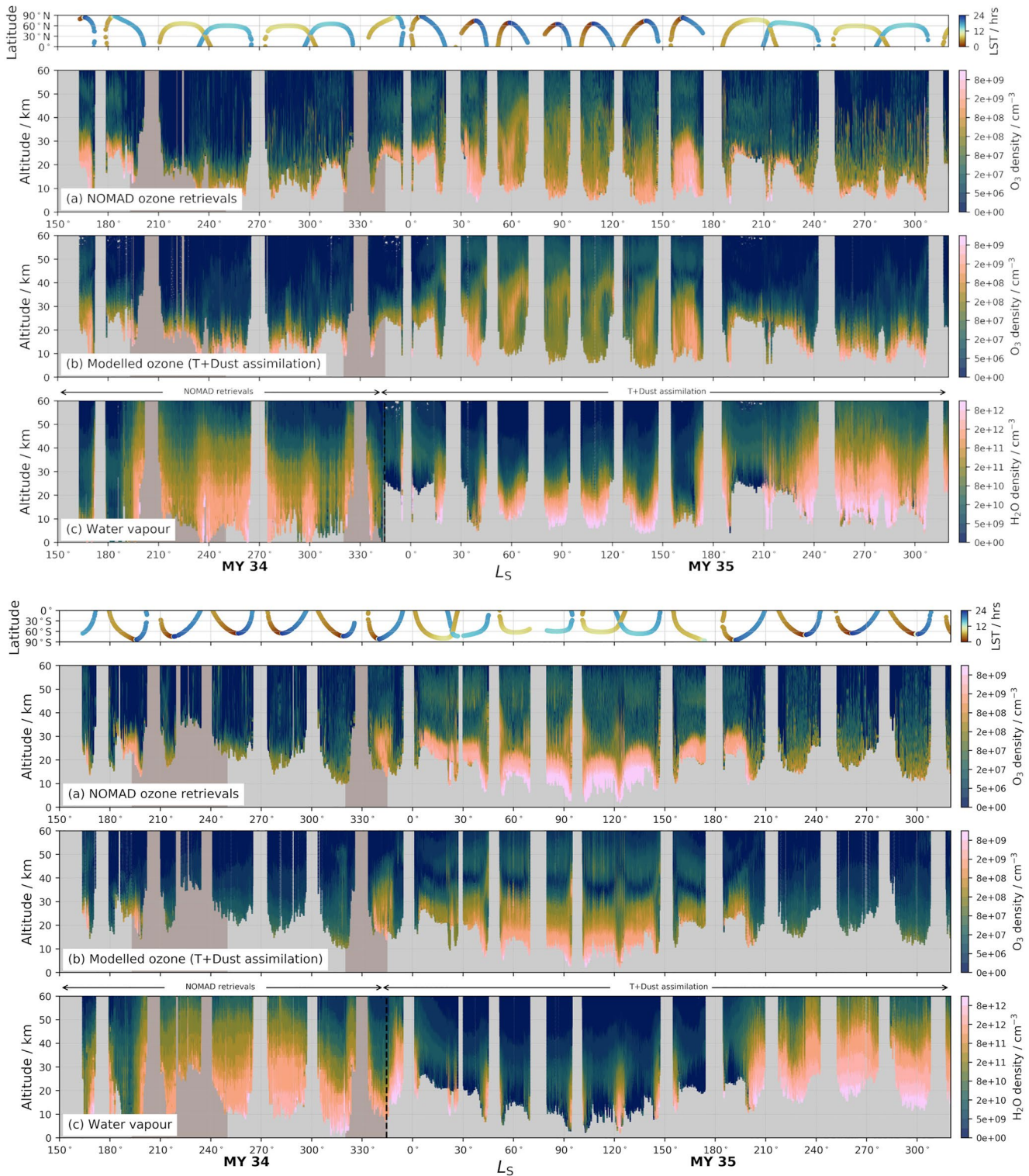
Figure 7. (top) Northern hemisphere altitude profiles for (a) NOMAD retrievals of O_3; (b) modeled O_3 based on initial conditions derived from SPICAM observations and evolved through time considering assimilated temperature and dust observations from MCS; (c) retrieved and modeled H_2O abundances (H_2O is modeled after $L_S = 345°$). NOMAD retrievals of H_2O are from Aoki et al. (2019). (bottom) The equivalent as above, but for the southern hemisphere. The UVIS O_3 retrieval profiles cover the period $L_S = 163°$ in MY34 to $L_S = 320°$ in MY35 and consist of 5,990 individual profiles and 677,473 individual spectra. The wide and narrow shaded periods represent the timing of the MY34 global dust storm and regional storm respectively. Altitude values are with reference to the Mars areoid, and the latitude that each profile is taken at is indicated by the top plot.

The bottom panels of Figure 7 present this NOMAD-model composite description of water profiles corresponding (in position and L_S) to retrieved NOMAD O_3 profiles in the top panels. It should be noted that the average difference in time between the model output time and each specific observation time is 12 min. This provides a partial comparison of NOMAD water vapor and O_3 profile measurements, for the published dust storm period of NOMAD observations (L_S = 190°–345° in MY34). It also allows a predictive (model) description of the very distinct behavior of Mars water vapor centered on the aphelion climate of Mars (L_S ∼0°–180°) in MY35.

NOMAD-retrieved O_3 profiles are presented in the top panels of Figure 7 and compared to simulated O_3 profiles in the middle panels. These simulated O_3 profiles are strictly based on the MCS temperature and dust assimilation modeling described above. Consequently, they correspond to modeled, not observed, atmospheric water vapor distributions for the entire presented L_S range in Figure 7. These simulated water vapor profiles are constrained by assimilated MCS temperature and dust profiles, as described above, such that they more closely correspond to contemporaneous water vapor saturation conditions, including the MY34 dust storm, high-latitudes, and the aphelion period.

Nevertheless, the model-NOMAD comparisons for O_3 profiles in the top two panels of Figure 7 still retain significant uncertainties associated with GCM simulations of Mars water vapor (Daerden et al., 2019; Navarro et al., 2014). Direct assimilation of NOMAD retrieved H_2O profiles should allow much more quantitatively direct (and photochemically diagnostic) comparisons of model and observed O_3 profiles. For current purposes, these model/data O_3 comparisons allow a preliminary assessment of the detailed seasonal and spatial variations of the vertical distribution of Mars O_3 from NOMAD, in the context of a best-effort approach for modeling Mars atmospheric water profile behavior based on assimilated dust and temperature profiles.

The effect of the MY34 global dust storm (approximately L_S = 190°–250°) on the O_3 retrievals, through reduced limb transmission, is most noticeable in the increasing lower altitude cut-off due to the sharp increases in dust loading (e.g., Liuzzi et al., 2020; Montabone et al., 2020; Smith, 2019). In the equatorial and mid-latitudes, retrievals are only possible down to ∼30 km, allowing only mid-to-upper level regions of atmospheric O_3 to be detected. At higher latitudes, where lower dust content is present, O_3 retrievals are possible to altitudes below 10–20 km. Elevated water abundances at high altitudes (>30–50 km) are observed in both northern and southern hemispheres during the MY34 (2018) global dust storm after L_S = 190°–200° (Aoki et al., 2019; Fedorova et al., 2020), similar to behavior observed and modeled during the MY28 (2007) global dust storm (Heavens et al., 2018). This leads to correspondingly reduced O_3 abundances above 20–30 km between L_S – 200°–300° in both hemispheres, in both MYs, associated with the strong photochemical anti-correlation between O_3 and water. As noted previously, the high-altitude enhancements of O_3 observed in the southern hemisphere (and to a lesser extent the northern hemisphere) from spring equinox are covered in detail in the companion article to this study (Khayat et al., 2021) and are not discussed here. A comparison of the difference in MY34/35 O_3 distribution during the global dust storm period is given in Section 4.3; however, care must be taken when comparing periods in Figure 7, since the latitude of the observations vary significantly and will be different between Mars Years.

Altitude-resolved NOMAD O_3 abundances below 15 km altitudes represent new measurements and will prove significant in assessing previous column (nadir) measurements of Mars ozone (e.g., Perrier et al., 2006). Such column measurements are often dominated by maximum lower atmospheric O_3 abundances, particularly at high-latitudes, that may contribute disproportionately to existing model-data disagreements for column O_3 comparisons (Clancy et al., 2016). Peak near-surface O_3 densities (and mixing ratios) are generally observed to be present throughout the Mars Year and occur, in part, due to reduced HO_x production from H_2O UV photolysis (associated with increasing CO_2 extinction of UV radiation, e.g., Montmessin & Lefèvre, 2013).

This near-surface O_3 layer is particularly evident at southern winter latitudes, when cold aphelion temperatures lead to the aphelion cloud belt (ACB) and much-reduced transport of water vapor into the southern winter hemisphere (Clancy et al., 1996), and thus minimum HO_x loss rates for O_3 at all altitudes (Daerden et al., 2019; Lefèvre et al., 2004). Figure 7 demonstrates this behavior in, respectively, NOMAD retrievals and assimilation modeling of O_3 and H_2O abundances in the southern hemisphere lower atmosphere
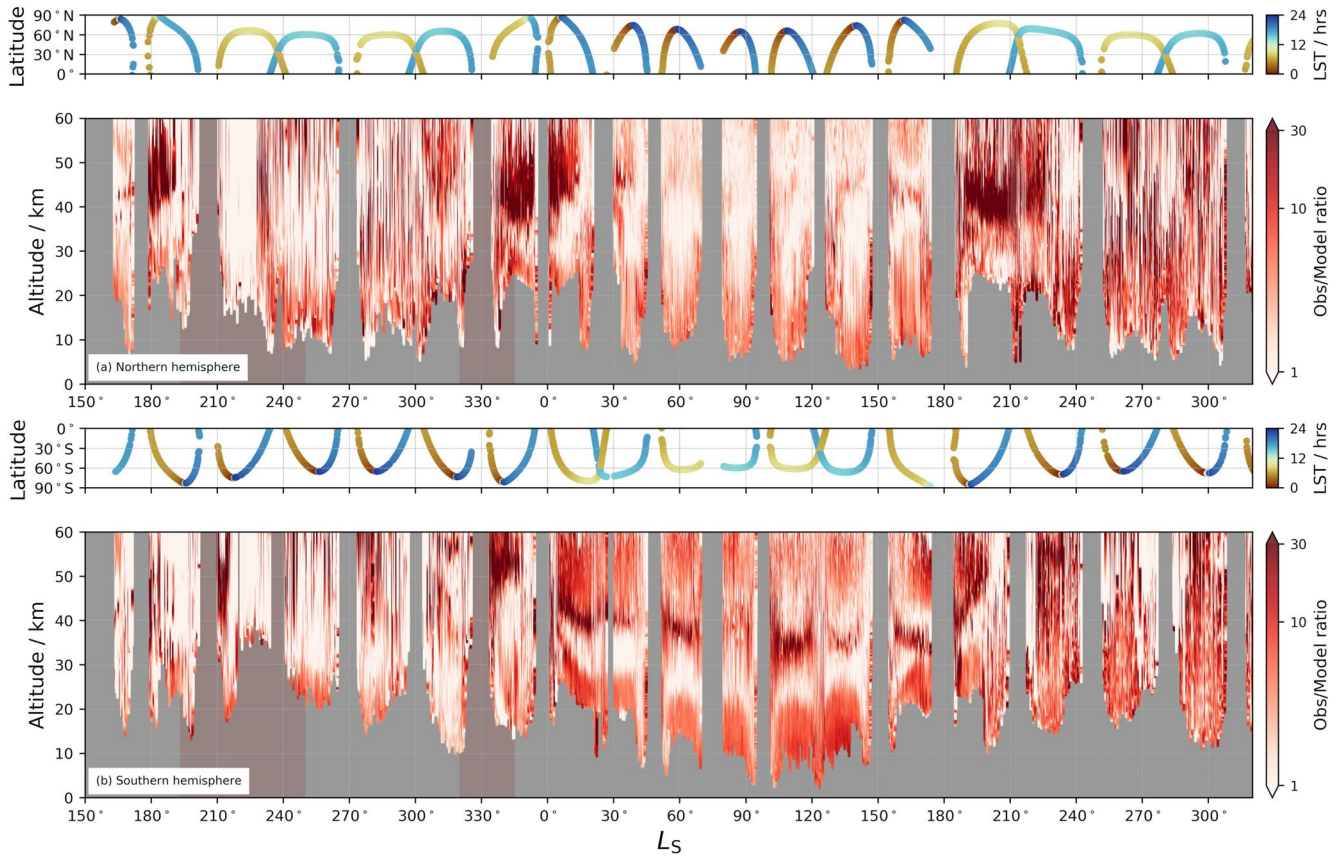
Figure 8. Ratio of the observed to modeled ozone abundance shown in Figure 7 for (a) the northern hemisphere and (b) the southern hemisphere. Lighter (darker) shading indicates stronger (weaker) agreement between observation and model abundances; higher ratio values indicate that modeled values are lower than that observed by NOMAD.

($L_S = \sim 0°-180°$). The northern hemisphere winter is generally obscured due to the presence of dust from the MY34 global dust storm. Increasing O_3 abundances below ~ 15 km altitudes are retrieved between $L_S = 190°-250°$, associated with northern winter. But overall, reduced O_3 and increased H_2O abundances (both, in this case, from NOMAD retrievals) are present relative to the aphelion, southern winter period.

Figure 8 shows the ratio of the O_3 abundance observed by NOMAD, to that simulated by the GCM following assimilation of MCS dust and temperature observations. Overall, there are periods/altitudes of both good and poor agreement between observation and model. The period $L_S = 200°-300°$ in general shows a good agreement in modeled O_3, compared to observation, when little O_3 is present. For example, at $L_S = 210°-240°$ in the northern hemisphere (i.e., during the global dust storm) there is an approximate unity observation/model ratio over most altitudes. A similar situation occurs at $L_S = 180°-200°$ in the southern hemisphere, with approximate unity observation-model ratio above ~ 35 km. Around aphelion in the northern hemisphere, there are generally low observation/model O_3 ratio values over all altitudes. In the southern hemisphere during this period, there are higher observation/model ratio values above and below the 25–35 km altitude range, with a sharp increase in ratio value around 35–40 km at the base of the enhanced O_3 layer.

Figure 7 showed that the qualitative distribution of O_3, including the structure and timing of the high-latitude, high altitude peaks, is represented well by the GCM. However, Figure 8 shows that, in general, while there can be a good agreement with the absolute abundances simulated in the GCM, there are also periods and altitudes when the GCM values are over a factor of 10 lower than that observed by NOMAD. This is most likely due to the fact that the water saturation conditions are only partially constrained by the temperature and dust assimilation, such that water abundances are not adequately represented in the model simulations (early on, water abundances from the assimilation of temperature and dust from MCS are approximately a factor of $\times 2$ higher than those observed by NOMAD). It is also likely that there are deficiencies

in our understanding of the HO_x processes in the atmosphere of Mars (see e.g., Lefèvre et al., 2021), which could contribute to such a discrepancy in O_3 abundance. Model assimilation of the observed NOMAD water profiles, once publicly available, will address this modeled O_3 abundance deficiency.

4.2. Latitudinal Distribution

Figure 9 shows the NOMAD ozone profile retrievals, plotted as a function of latitude for L_S periods of 20°. Toward perihelion ($L_S = 251°$) in northern winter, O_3 is generally present at low altitudes at mid/high-latitudes. A comparison of the northern autumnal equinox periods for MY34 and MY35 ($L_S = 160°–180°$ and 180°–200°) indicates that observed O_3 abundances extend to higher altitudes in the non-global dust storm year (MY35). Mid/high-latitude O_3 abundances above ∼20 km are reduced during the MY34 global dust storm, due to the elevated water abundance above these altitudes associated with this storm (e.g., Aoki et al., 2019; Fedorova et al., 2020). The period $L_S = 180°–200°$ presents an especially high number of observations in both years, and thus is most appropriate for this comparison. In MY34 during this period, O_3 reaches an altitude of 20–30 km in the southern polar regions, at the onset of the global dust storm. In the MY35 equivalent period, O_3 reaches an altitude of 30–40 km, highlighting the reduction of O_3 abundances in this region in MY34 associated with dust-driven increases in water vapor at higher altitudes. Northern mid-latitudes (∼30°–45°N) also exhibit higher O_3 abundances in the $L_S = 180°–200°$ period in MY35 with respect to MY34, but limited observations during the MY34 period make it difficult to compare this latitude region further. Following cessation of the regular period of dust activity centered near $L_S = 330°$ in MY34 (e.g., Kass et al., 2016; Smith, 2004), the development of increased O_3 abundances to altitudes of ∼35 km is observed in the southern polar regions in MY34 at $L_S = 340°–0°$).

The notable low-to-mid latitude increases in 20–50 km altitude O_3 over the extended northern summer season ($L_S = 40°–120°$) reflect the aphelion saturation conditions for water vapor above ∼20 km altitudes. This orbitally driven cooling of the global Mars atmosphere leads to the formation of the ACB (Clancy et al., 1996; Montmessin et al., 2004; Smith, 2004) and sharp increases in O_3 abundances above 20 km (Clancy & Nair, 1996; Lefèvre et al., 2004) at this time. These vertically extended increases in aphelion O_3 abundances continue until L_S ∼120°, after which O_3 abundances above 20–30 km begin to decrease with increasing atmospheric temperatures and water vapor. The ACB similarly declines over this period (Smith, 2004).

At $L_S = 40°–60°$ in Figure 9, meridional circulation during the transition from equinoctial to solstitial circulation is evident in the latitudinal O_3 distribution, where O_3 formation along the flow path of O atoms highlights the meridional circulation. The downwelling branch of the main Hadley cell typical of this time of year (e.g., Barnes et al., 2017; Montmessin & Lefèvre, 2013) shapes the O_3 distribution in the southern hemisphere and manifests as a latitudinal contour of O_3 abundance beginning at a latitude of ∼30°S and altitude of ∼45 km down to a latitude of ∼55°S and altitude of 20 km. There is evidence of a thermally indirect (Ferrel) cell at high northern latitudes at altitude, manifesting as an O_3 abundance contour extending from a latitude of ∼50°N and 30 km down to a latitude of ∼70°N and ∼20 km. Progressing toward solstitial circulation, in the $L_S = 60°–80°$ period there is a possible signature of the elevation of the thermally indirect (Ferrel) cell flow path, being elevated by approximately 10–15 km, with the O_3 contour highlighting the circulation flow path spanning from a latitude of ∼35°N at 45 km down to ∼65°N at ∼30 km. It should be noted that the meridional circulations highlighted here do not represent the strength or extent of the circulation nor the transport of O_3, but serve only to highlight the (possibly weak) circulation paths where the formation of sufficient O_3 is permitted and thus made observable.

4.3. O_3 Distribution Compared to H_2O

O_3 and H_2O are always photochemically anti-correlated in terms of HO_x chemistry. Care must be taken when using the terms "correlated" and "anti-correlated" in studies such as presented here, to avoid misunderstanding regarding the relationship between O_3 and H_2O. While these two species are fundamentally anticorrelated from a chemical reaction perspective, the variation of these species over altitude is not necessarily constrained in the same manner. For example, it is possible for both O_3 and H_2O to follow the same decrease in relative abundance over altitude, while remaining photochemically anti-correlated. Competing photochemical processes will dominate at different altitudes (e.g., solar UV at high altitudes enhancing
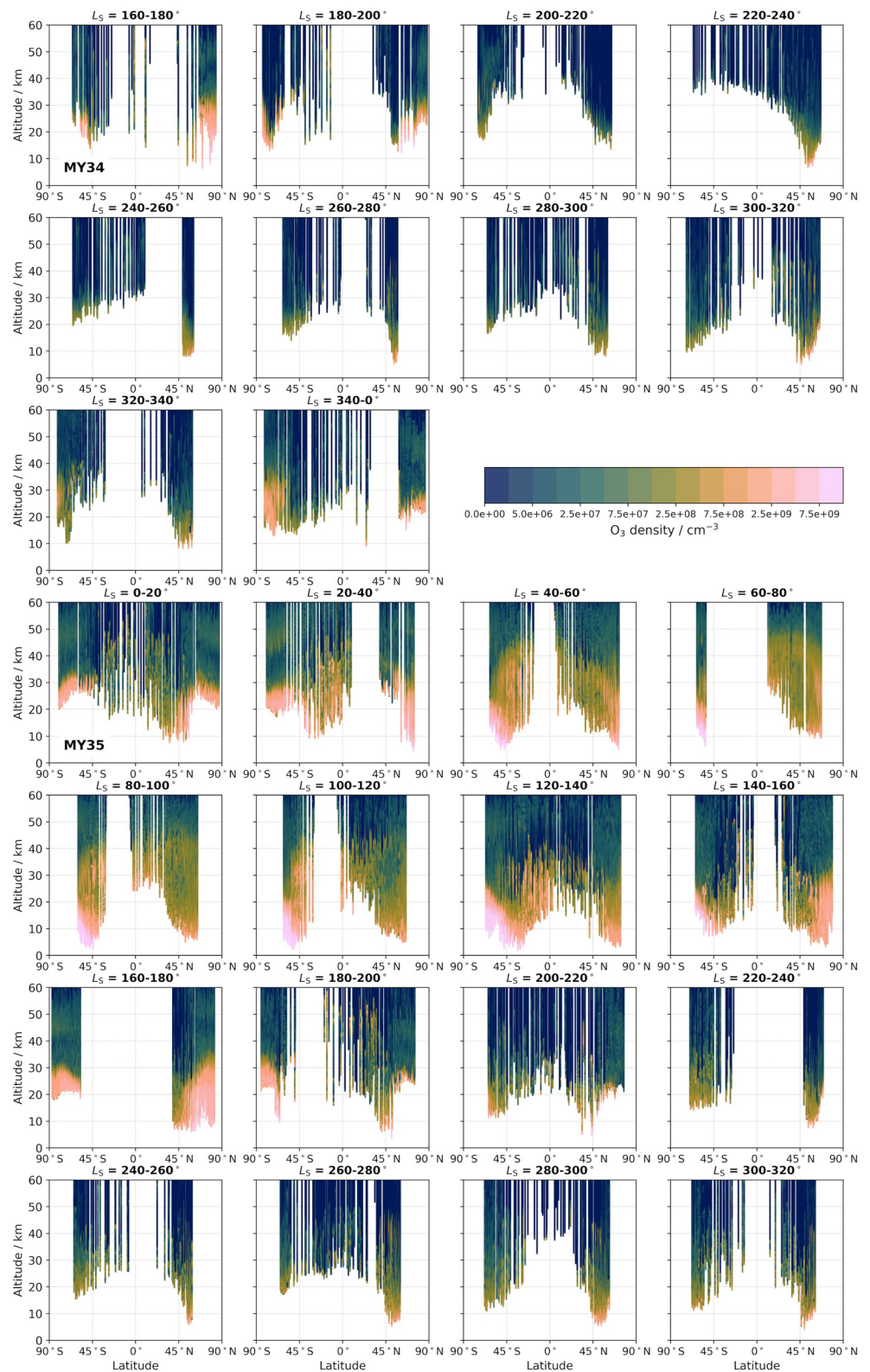
Figure 9. Latitudinal distribution of the NOMAD O_3 retrievals over 1 Martian year. Each plot shows the vertical profiles obtained during an $L_S = 20°$ period.

destruction pathways and reducing in effectiveness toward the surface). A common assumption that follows the statement of anti-correlation between the two species is that their profile shapes will also be anti-correlated—this is not necessarily always the case. NOMAD is capable of measuring simultaneously O_3 and H_2O vapor profiles to demonstrate this through observations; here we discuss the relationship of the two species regarding their relative vertical distribution.

Figure 10 presents the comparison of O_3 and H_2O as a function of altitude and latitude. Figure 10 shows the distribution of NOMAD O_3 and H_2O retrievals from $L_S = 163°$ onwards for the remainder of MY34, and also the NOMAD O_3 compared to the modeled O_3 (following MCS dust and temperature assimilation) for MY35 up to $L_S = 280°$.

At perihelion in MY34 between $L_S = 200°–320°$ there is a greater relative density of NOMAD-retrieved H_2O, particularly at high altitudes (>30 km) in both hemispheres, due to the ~20 K increase in average atmospheric temperatures associated with the ~40% increase in solar flux (Clancy et al., 1996), and due to the related intense dust activity during the global and regional storms (Liuzzi et al., 2020; Smith, 2019). During this period, O_3 is confined to lower altitudes, with the altitude of peak O_3 values in general being coincident with peak H_2O values. O_3 and H_2O show a similar overall trend in increasing relative abundance with decreasing altitude. Either side of this period (i.e., $L_S = 160°–200°$ and $320°–0°$), water abundance is generally lower, and distinct increased O_3 abundance is observed at high-latitudes in both hemispheres, coincident with latitudes where H_2O abundances are decreased. This anti-correlation in distribution continues into MY35, with the latitudinal anti-correlation immediately evident in the $L_S = 0°–40°$ period, and continuing albeit to a lesser degree throughout the rest of the year.

Toward aphelion in MY35 during the northern summer there is an overall lower density of modeled H_2O, and a higher density of O_3, consistent with the generally colder aphelion season due to decreased solar insolation and dust loading. In MY35, O_3 retrievals were possible to lower altitudes than in MY34 due to the absence of storm-related high dust loading. From $L_S = 0°–160°$, H_2O is confined below 40 km in both hemispheres, showing dry south polar regions to the minimum altitudes observed by NOMAD (~5–10 km). From $L_S = 40°–120°$, O_3 density is consistently high across all latitudes up to altitudes of ~50 km, consistent with the generally low H_2O densities in these regions. At $L_S = 120°–160°$ H_2O abundances increase across all latitudes, shifting the abundances upwards by ~5 km in altitude. This general increase in H_2O at high altitudes results in a corresponding decrease in O_3, showing an anti-correlation with the H_2O distribution across latitudes and above 30 km. With the reappearance of the high-latitude, high altitude O_3 enhancement >40 km, no corresponding H_2O peak is seen below the O_3 enhancement, as observed during the vernal equinox.

Figure 11 shows a sample comparison of several coincident NOMAD O_3 and H_2O profiles (top row = NOMAD H_2O observations, bottom row = assimilation model profiles). These profiles cover the time period $L_S = 213.3°$ (MY34) to $L_S = 165.8°$ (MY35), at high-latitudes (up to 83.2°S). In MY34 through perihelion, the relative abundance of both O_3 and H_2O increases coherently toward the surface with peak values of both species occurring at the lowest altitudes, consistent with the build-up of O_3 at lower altitudes attributed to the reduced H_2O photolysis rates arising from the overlying CO_2 atmosphere and the increase in efficiency of the three-body ozone forming reaction at lower altitudes (higher pressures; Montmessin & Lefèvre, 2013). In MY35 through aphelion, H_2O profiles show an inflection around 20–30 km, resulting in maximum H_2O abundances occurring at higher altitudes than during perihelion. O_3 profiles show a sharp drop at the point of the H_2O maxima. While the photochemical anti-correlation of O_3 and H_2O remains valid throughout the Martian year, there is a clear difference in the shape of the H_2O profiles between the warmer, wetter perihelion season and the colder, drier aphelion season. The top row in Figure 11 shows the O_3 and H_2O vertical profile shapes at high-latitudes in the southern summer, whereas the bottom row demonstrates the equivalent profiles for similar latitudes located in the southern polar vortex. For the latter, the higher altitude O_3 enhancements are created through the descent of O atoms via Hadley circulation (Montmessin & Lefèvre, 2013), altering the shape of the profile with respect to the southern summer period. Direct NOMAD O_3-H_2O comparisons in MY35 should confirm these observations in detail. Furthermore, assimilating retrieved NOMAD H_2O profiles are expected to lead to much better O_3 absolute abundance simulations, which often appear lower than NOMAD measurements (Figure 8).
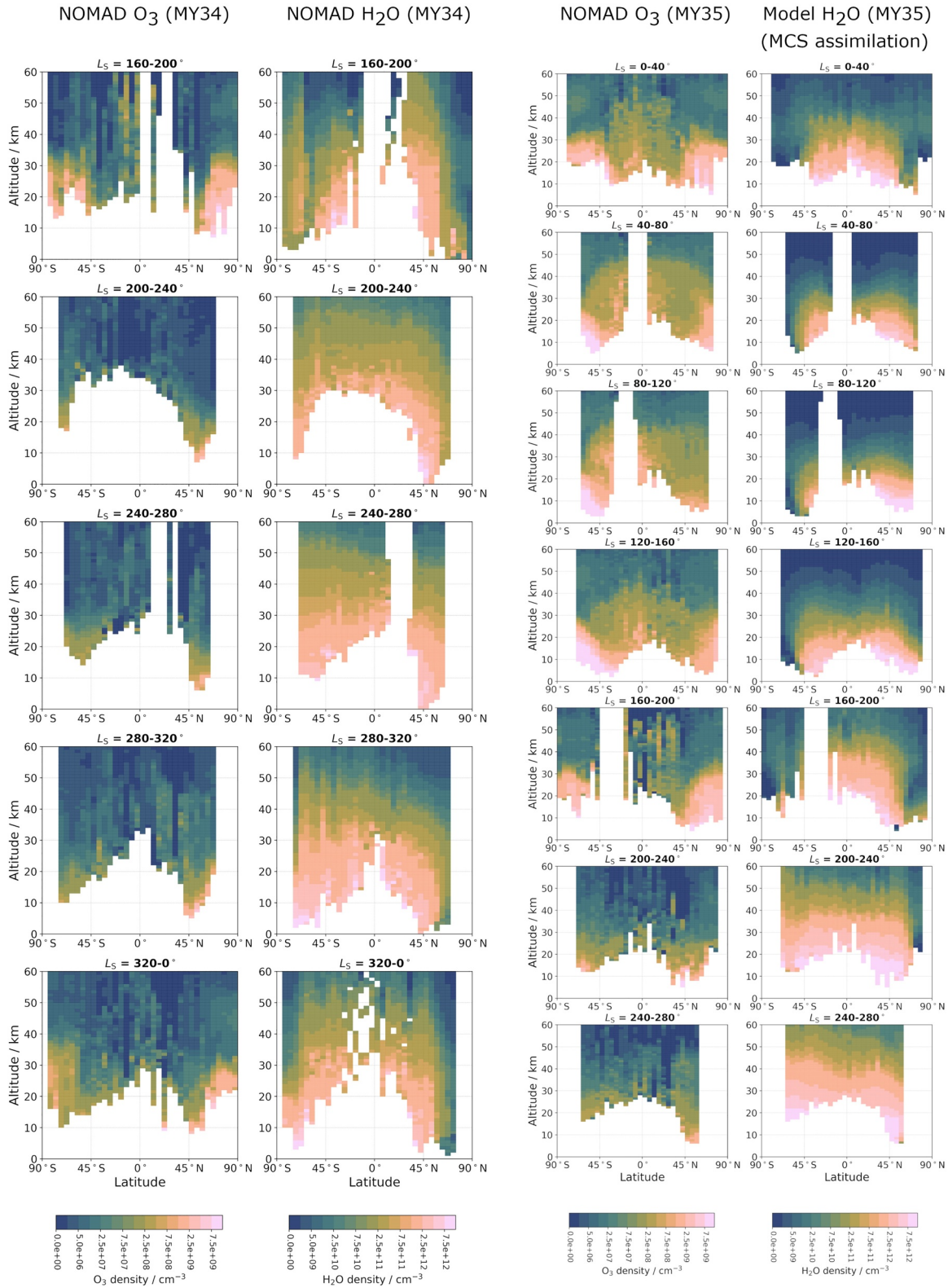
Figure 10. Latitudinal distribution comparison of (left column pair) NOMAD O_3 retrievals and (right column) NOMAD H_2O retrievals (Aoki et al., 2019), in L_S intervals of 40° during MY34, and (right column pair) as left pair but for MY35, and with assimilated model output for H_2O. Retrievals are binned every 5° latitude and 1 km altitude for clarity. The same color scale is used for both species, with different absolute scales.
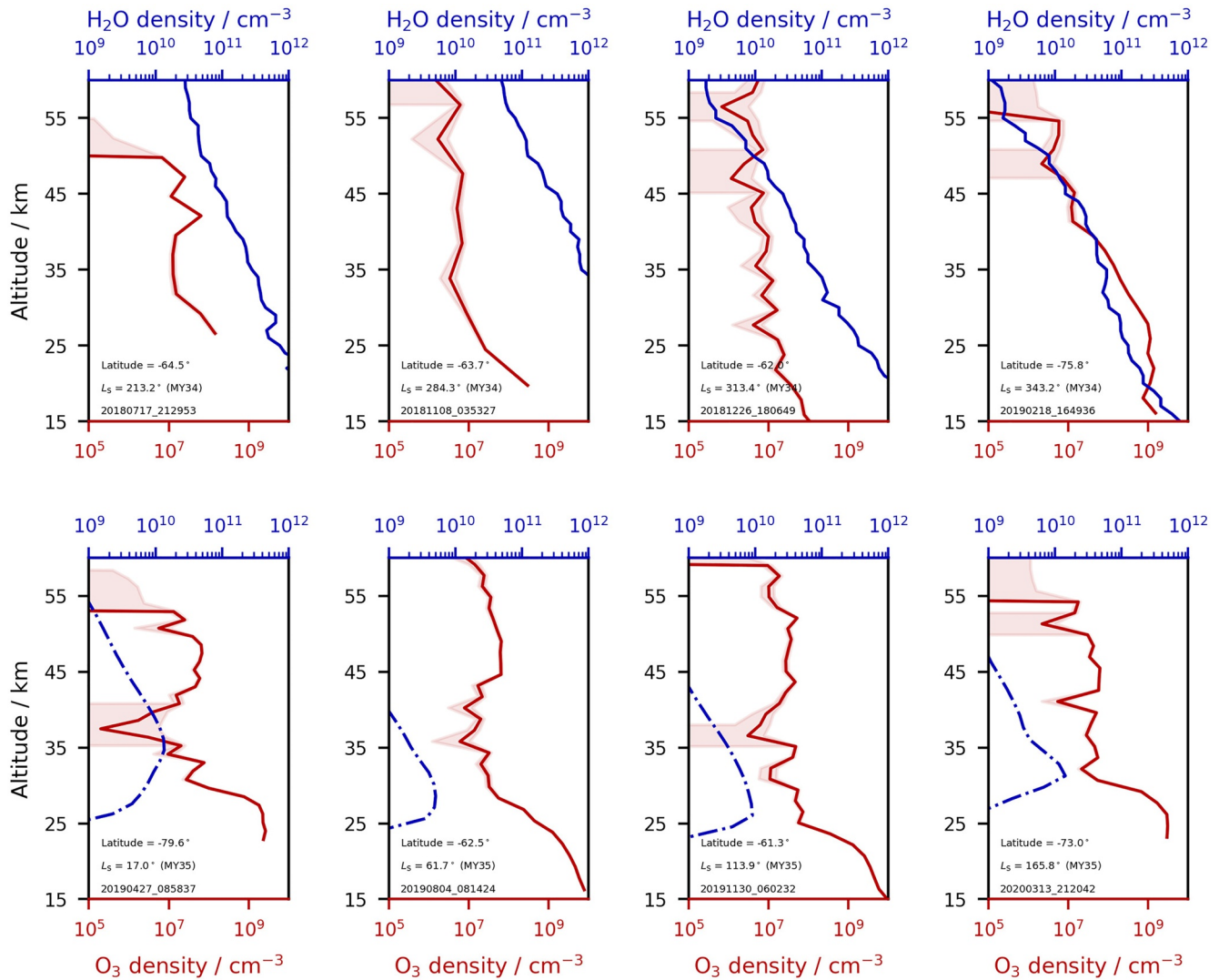
Figure 11. Vertical profiles of O_3 and H_2O. Top row shows a comparison of NOMAD O_3 and NOMAD H_2O retrievals, bottom row shows a comparison of NOMAD O_3 with modeled H_2O from the MCS dust/temperature assimilation. These profiles cover the period $L_S = 213.3°$ MY34 to $L_S = 165.8°$ MY35. The observation data filename, L_S, and latitude are shown in each sub-plot.

4.4. Night-to-Day and Day-to-Night Terminator Perspectives

A key feature of the non-Sun-synchronous orbit of TGO is that it allows NOMAD to observe different local times of day on Mars. This benefit is key to NOMAD nadir observations, which enable total column measurements at varying local times across the planet. Whilst occultation observations are also made at differing local times as a function of latitude and season, by definition an occultation observation always occurs at local sunrise/sunset, at the terminator. Interpreting fine-scale diurnal variations in NOMAD occultation data should be done with care, since occultation measurements will always be performed with the observation tangent point at the day/night boundary, and do not represent the diurnal mean ozone profile.

It is valid, however, to draw conclusions on the difference between sunrise and sunset occultations. From the perspective of viewing geometry, the TGO spacecraft is in eclipse behind Mars prior to a sunrise occultation; the NOMAD-Sun LoS, therefore, transects the atmosphere that is emerging from the nightside conditions of Mars for a sunrise occultation. For a sunset occultation, the opposite is true, where TGO points toward the Sun after passing over the dayside of Mars. For a sunset occultation, the NOMAD-Sun LoS, therefore, transects the atmosphere that has been subjected to the dayside conditions of Mars (high
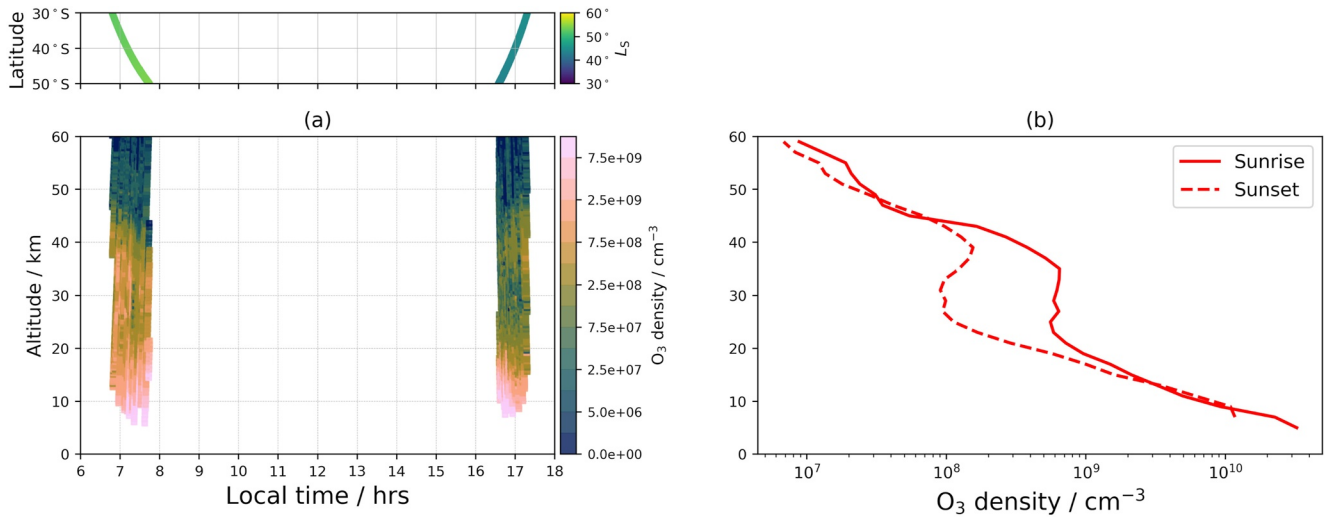
Figure 12. Sunrise and sunset occultations showing the O_3 vertical profile number density for (a) individual profiles over the period $L_S = 42°–54°$ and the latitude range 30°–50°S, and (b) the average of these profiles split by sunrise and sunset observation geometry. The exact latitude and L_S for each profile is shown above the plot.

temperatures, solar UV). Both cases will consist of observations with part-night/part-day optical paths, with the difference being the exposure period of each optical path to day/night conditions.

Figure 12 shows the vertical profiles for a group of observations between $L_S = 42°–54°$, and latitude range 30°–50°S. Whilst local time is plotted, this serves primarily to discriminate between sunrise and sunset occultations, to discern the differences between the nightside and dayside atmospheric "context" of the occultations.

In Figure 12a, the sunrise occultations show an O_3 number density at approximately 10^9 cm^{-3} up to an altitude of ~35 km. This is in stark contrast to the equivalent sunset occultations, where the equivalent number density only reaches an altitude of ~20 km. Figure 12b shows this striking distinction, with the profile averages for sunset and sunrise during this period at similar values above ~45 km and below ~15 km but showing vastly different abundances between these altitudes. The relative shape of the distribution between 20 and 40 km is similar, but the abundance of O_3 is an order of magnitude higher at sunrise than at sunset. Figure 12 thus shows a clear bias toward higher O_3 abundances at sunrise for altitudes between 15 and 45 km than for equivalent sunset occultations within the same period. This difference could arise from diurnal partitioning between O_3 and O, which leads to nighttime conversion of O to O_3 when O_3 photolysis is inactive, resulting in significant O_3 increases above 20–30 km altitudes associated with altitude increasing O densities (e.g., Nair et al., 1994). Day-time photolysis of O_3 to O leads to reduced O_3 densities above 20–30 km. Consequently, the photolysis-driven diurnal partitioning of O_3 and O can plausibly create the observed sunrise and sunset O_3 profile variations indicated in Figure 12a. However, the occultation atmospheric paths transect day and night illuminated regions at both terminators, and diurnal O_3 variations associated with O_3 partitioning are not instantaneous at the terminators. Previous studies have investigated diurnal changes in O_3 from a model perspective (e.g., Holmes et al., 2018), however a photochemistry model investigation of the diurnal variation of ozone is beyond the scope of this article. Additionally, it should be noted that the measurements shown in Figure 12 are not made at precisely the same local time and L_S, and there is a possibility that the water vapor profile abundance has changed over the short period of ~3 weeks for the observations in Figure 12, and the difference could therefore be driven by differences in the water profile between sunrise and sunset. Comparison to NOMAD water profile observations is unfortunately not possible at the present time, but once available, detailed photochemical modeling is planned to assess these NOMAD sunrise-sunset distinctions which should yield new constraints on Mars photochemistry.

5. Conclusions

We have analyzed the first Martian year of occultation observations from the NOMAD instrument on ExoMars TGO and presented a new climatology of the vertical distribution of O_3 for the period $L_S = 163°$ in MY34 to $L_S = 320°$ in MY35. The vertical, latitudinal, and seasonal (L_S) variations of these retrieved NOMAD O_3 profiles are compared with coincident NOMAD H_2O profiles obtained during the MY34 global dust storm (Aoki et al., 2019), and to OU data assimilation modeling of O_3 and H_2O profiles, in which MCS temperature and dust profiles are assimilated to constrain water vapor saturation conditions.

These NOMAD O_3 profile retrievals present the first detailed, global description of Mars O_3 vertical distributions as a function of season and latitude, and with accurate sensitivity from below 10 km (depending on variable atmospheric aerosol extinction) to above 50 km (depending on variable O_3 abundance) altitudes. Key global-scale variations in Mars atmospheric O_3 are well characterized in their vertical extents, including: large aphelion ($L_S = 40°–120°$) increases in low-to-mid latitude O_3 abundances over 20–50 km altitudes, distinct high-latitude ($>\pm55°$), high altitude (40–55 km) enhancements in O_3 abundances during equinoctial seasons (centered on $L_S = 0°, 180°$), and very large perihelion O_3 decreases over the extended atmosphere. The aphelion increases and perihelion decreases are generally consistent with model predictions of global variation in water vapor saturation altitudes (hygropause) as driven by the elliptical Mars orbit and accentuated by perihelion dust storm heating of the extended atmosphere. During perihelion, the relative vertical abundances of O_3 and H_2O increases below ~40 km toward the surface, with both species having peak abundances at similar altitudes close to the surface; during aphelion, the same general trend applies, but with well-defined decreases in O_3 abundances present in the profiles at altitudes of 20–30 km, coincident with local peaks in H_2O. Between L_S 40° and 50° in MY35, the difference in O_3 abundance between 20 and 40 km was found to be on average an order of magnitude higher at the sunrise terminator, compared to the sunset terminator.

In general, modeled O_3 densities are either in agreement with or lower than NOMAD observed O_3 densities, most likely due to H_2O abundance conditions being inadequately constrained in the model without significant tuning. An in-progress objective of assimilating NOMAD water profile measurements should provide the most diagnostic photochemical analysis of Martian O_3, necessary to accurately represent the formation and distribution of O_3 on Mars.

Data Availability Statement

Public access to the derived ozone retrieval data data set and the modeling and assimilation data that support the plots within this article are available through the following data citation reference: Patel (2021).

References

Aoki, S., Vandaele, A. C., Daerden, F., Villanueva, G. L., Liuzzi, G., Thomas, I. R., et al. (2019). Water vapor vertical profile on Mars in dust storms observed by TGO/NOMAD. *Journal of Geophysical Research: Planets*, 124, 3482–3497. https://doi.org/10.1029/2019JE006109

Auvinen, H., Oikarinen, L., & Kyrölä, E. (2002). Inversion algorithms for recovering minor species densities from limb scatter measurements at UV-visible wavelengths. *Journal of Geophysical Research*, 107, D13. https://doi.org/10.1029/2001JD000407

Barnes, J., Haberle, R., Wilson, R., Lewis, S., Murphy, J., & Read, P. (2017). The global circulation. In R. Haberle, R. Clancy, F. Forget, M. Smith, & R. Zurek (Eds.), *The atmosphere and climate of Mars (Cambridge Planetary Science* (pp. 229–294). Cambridge University Press. https://doi.org/10.1017/9781139060172.009

Barth, C. A., & Hord, C. W. (19711971). Mariner ultraviolet spectrometer: Topography and polar cap. *Science*, 173, 197–201. https://doi.org/10.1126/science.173.3993.197

Barth, C. A., Hord, C. W., Stewart, A. I., Lane, A. L., Dick, M. L., & Anderson, G. P. (1973). Mariner 9 ultraviolet spectrometer experiment: Seasonal variation of ozone on Mars. *Science*, 179(4075), 795–796. https://doi.org/10.1126/science.179.4075.795

Bellucci, A., Sicardy, B., Drossart, P., Rannou, P., Nicholson, P. D., Hedman, M., et al. (2009). Titan solar occultation observed by Cassini/VIMS: Gas absorption and constraints on aerosol composition. *Icarus*, 201, 198–216. https://doi.org/10.1016/j.icarus.2008.12.024

Bétrémieux, Y., & Kaltenegger, L. (2015). Refraction in planetary atmospheres: Improved analytical expressions and comparison with a new ray-tracing algorithm. *Monthly Notices of the Royal Astronomical Society*, 451(2), 1268–1283. https://doi.org/10.1093/mnras/stv1078

Blamont, J. E., & Chassefière, E. (1993). First detection of ozone in the middle atmosphere of Mars from solar occultation measurements. *Icarus*, 104(2), 324–336. https://doi.org/10.1006/icar.1993.1104

Clancy, R. T., Grossman, A. W., Wolff, M. J., James, P. B., Billawala, Y. N., Sandor, B. J., et al. (1996). Water vapor saturation at low altitudes around Mars aphelion: A key to Mars climate? *Icarus*, 122, 36–62. https://doi.org/10.1006/icar.1996.0108

Clancy, R. T., & Nair, H. (1996). Annual (perihelion-aphelion) cycles in the photochemical behavior of the global Mars atmosphere. *Journal of Geophysical Research: Planets*, 101(E5), 12785–12790. https://doi.org/10.1029/96je00836

Clancy, R. T., Smith, M. D., Lefèvre, F., McConnochie, T. H., Sandor, B. J., Wolff, M. J., et al. (2017). Vertical profiles of Mars 1.27 μm O_2 dayglow from MRO CRISM limb spectra: Seasonal/global behaviors, comparisons to LMDGCM simulations, and inferences on Mars water vapor distributions. *Icarus*, *293*, 132–156. https://doi.org/10.1016/j.icarus.2017.04.011

Clancy, R. T., Wolff, M. J., & James, P. B. (1999). Minimal aerosol loading and global increases in atmospheric ozone during the 1996–1997 Martian northern spring season. *Icarus*, *138*, 49–63. https://doi.org/10.1006/icar.1998.6059

Clancy, R. T., Wolff, M. J., Lefèvre, F., Cantor, B. A., Malin, M. C., & Smith, M. D. (2016). Daily global mapping of Mars ozone column abundances with MARCI UV band imaging. *Icarus*, *266*, 112–133. https://doi.org/10.1016/j.icarus.2015.11.016

Colaïtis, A., Spiga, A., Hourdin, F., Rio, C., Forget, F., & Millour, E. (2013). A thermal plume model for the Martian convective boundary layer. *Journal of Geophysical Research*, *118*, 1468–1487.

Daerden, F., Neary, L., Viscardy, S., García Muñoz, A., Clancy, R. T., Smith, M. D., et al. (2019). Mars atmospheric chemistry simulations with the GEM-Mars general circulation model. *Icarus*, *326*, 197–224. https://doi.org/10.1016/j.icarus.2019.02.030

Fast, K., Kostiuk, T., Espenak, F., Annen, J., Buhl, D., Hewagama, T., et al. (2006). Ozone abundance on Mars from infrared heterodyne spectra: I. Acquisition, retrieval, and anticorrelation with water vapor. *Icarus*, *181*(2), 419–431. https://doi.org/10.1016/j.icarus.2005.12.001

Fedorova, A., Bertaux, J.-P., Betsis, D., Montmessin, F., Korablev, O., Maltagliati, L., & Clarke, J. (2018). Water vapor in the middle atmosphere of Mars during the 2007 global dust storm. *Icarus*, *200*, 440–457. https://doi.org/10.1016/j.icarus.2017.09.025

Fedorova, A., Korablev, O., Perrier, S., Bertaux, J.-L., Lefèvre, F., & Rodin, A. (2006). Mars water vapor abundance from SPICAM IR spectrometer: Seasonal and geographic distributions. *Journal of Geophysical Research Atmospheres*, *111*, E09S08. https://doi.org/10.1029/2006je002695

Fedorova, A., Montmessin, F., Korablev, O., Luginin, M., Trokhimovskiy, A., Belyaev, D. A., et al. (2020). Stormy water on Mars: The distribution and saturation of atmospheric water during the dusty season. *Science*, *367*, 297–300. https://doi.org/10.1126/science.aay9522

Forget, F., Hourdin, F., Fournier, R., Hourdin, C., Talagrand, O., Collins, M., et al. (1999). Improved general circulation models of the Martian atmosphere from the surface to above 80 km. *Journal of Geophysical Research*, *104*(E10), 24155–24175. https://doi.org/10.1029/1999je001025

Gröller, H., Montmessin, F., Yelle, R. V., Lefèvre, F., Forget, F., Schneider, N. M., et al. (2018). MAVEN/IUVS stellar occultation measurements of Mars atmospheric structure and composition. *Journal of Geophysical Research: Planets*, *123*, 1449–1483.

Guzewich, S. D., Lemmon, M., Smith, C. L., Martínez, G., de Vicente-Retortillo, Á., Newman, C. E., et al. (2019). Mars Science Laboratory observations of the 2018/Mars Year 34 global dust storm. *Geophysical Research Letters*, *46*, 71–79. https://doi.org/10.1029/2018GL080839

Heavens, N. G., Kleinböhl, A., Chaffin, M. S., Halekas, J. S., Kass, D. M., Hayne, P. O., et al. (2018). Hydrogen escape from Mars enhanced by deep convection in dust storms. *Nature Astronomy*, *2*, 126–132. https://doi.org/10.1038/s41550-017-0353-4

Holmes, J. A., Lewis, S. R., & Patel, M. R. (2017). On the link between Martian total ozone and potential vorticity. *Icarus*, *282*, 104–117. https://doi.org/10.1016/j.icarus.2016.10.004

Holmes, J. A., Lewis, S. R., & Patel, M. R. (2020). OpenMARS: A global record of Martian weather from 1999–2015. *Planetary and Space Science*, *188*, 1049462. https://doi.org/10.1016/j.pss.2020.104962

Holmes, J. A., Lewis, S. R., Patel, M. R., & Lefèvre, F. (2018). A reanalysis of ozone on Mars from assimilation of SPICAM observations. *Icarus*, *302*, 308–318. https://doi.org/10.1016/j.icarus.2017.11.026

Holmes, J. A., Lewis, S. R., Patel, M. R., & Smith, M. D. (2019). Global analysis and forecasts of carbon monoxide on Mars. *Icarus*, *328*, 232–245. https://doi.org/10.1016/j.icarus.2019.03.016

Hubbard, W. B., Fortney, J. J., Lunine, J. I., Burrows, A., Sudarsky, D., & Pinto, P. (2001). Theory of extrasolar giant planet transits. *The Astrophysical Journal*, *560*(1), 413–419. https://doi.org/10.1086/322490

Ityaksov, D., Linnartzm, H., & Ubachs, W. (2008). Deep-UV absorption and Rayleigh scattering of carbon dioxide. *Chemical Physics Letters*, *462*, 31–34. https://doi.org/10.1016/j.cplett.2008.07.049

Jakosky, B. M., & Farmer, C. B. (1982). The seasonal and global behavior of water vapor in the Mars atmosphere: Complete global results of the Viking Atmospheric Water Detector Experiment. *Journal of Geophysical Research*, *87*, 2999–3019. https://doi.org/10.1029/jb087ib04p02999

Kass, D. M., Kleinböhl, A., McCleese, D. J., Schofiled, J. T., & Smith, M. D. (2016). Interannual similarity in the Martian atmosphere during the dust storm season. *Geophysical Research Letters*, *43*, 6111–6118. https://doi.org/10.1002/2016gl068978

Khayat, A. S. J., Smith, M. D., & Guzewich, S. D. (2019). Understanding the water cycle above the north polar cap on Mars using MRO CRISM retrievals of water vapor. *Icarus*, *321*, 722–735. https://doi.org/10.1016/j.icarus.2018.12.024

Khayat, A. S. J., Smith, M. D., Wolff, M. J., Daerden, F., Neary, L., Patel, M. R., et al. (2021). ExoMars TGO/NOMAD-UVIS vertical profiles of ozone: Part 2: The high-altitude peaks of atmospheric ozone. *Journal of Geophysical Research: Planets*, *126*, e2021JE006834. https://doi.org/10.1029/2021JE006834

Kleinböhl, A., Friedson, A. J., & Schofield, J. T. (2017). Two-dimensional radiative transfer for the retrieval of limb emission measurements in the Martian atmosphere. *Journal of Quantitative Spectroscopy and Radiative Transfer*, *187*, 511–522.

Kong, T. Y., & McElroy, M. B. (1977). Photochemistry of the Martian Atmosphere. *Icarus*, *32*, 168–189. https://doi.org/10.1016/0019-1035(77)90058-6

Korablev, O., Olsen, K. S., Trokhimovskiy, A., Lefèvre, F., Montmessin, F., Fedorova, A. A., et al. (2021). Transient HCl in the atmosphere of Mars. *Science Advances*, *7*(7). https://doi.org/10.1126/sciadv.abe4386

Korablev, O., Vandaele, A. C., Montmessin, F., Fedorova, A. A., Trokhimovskiy, A., Forget, F., et al. (2019). No detection of methane on Mars from early ExoMars Trace Gas Orbiter observations. *Nature*, *568*, 517–520. https://doi.org/10.1038/s41586-019-1096-4

Lebonnois, S., Quémerais, E., Montmessin, F., Lefèvre, F., Perrier, S., Bertaux, J.-L., & Forget, F. (2006). Vertical distribution of ozone on Mars as measured by SPICAM/Mars Express using stellar occultations. *Journal of Geophysical Research: Planets*, *111*(E9). https://doi.org/10.1029/2005je002643

Lefèvre, F., Bertaux, J.-L., Clancy, R. T., Encrenaz, T., Fast, K., Forget, F., et al. (2008). Heterogeneous chemistry in the atmosphere of Mars. *Nature*, *454*, 971.

Lefèvre, F., & Krasnopolsky, V. (2017). Atmospheric photochemistry. In R. M. Haberle, R. Todd Clancy, F. Forget, M. D. Smith, & R. W. Zurek (Eds.), *The atmosphere and climate of Mars* (pp. 405–432). Cambridge University Press. (chapter 13).

Lefèvre, F., Lebonnois, S., Montmessin, F., & Forget, F. (2004). Three-dimensional modeling of ozone on Mars. *Journal of Geophysical Research: Planets*, *109*(E7).

Lefèvre, F., Trokhimovskiy, A., Fedorova, A., Baggio, L., Lacombe, G., Määttänen, A., et al. (2021). Relationship between the ozone and water vapor columns on Mars as observed by SPICAM and calculated by a global climate model. *Journal of Geophysical Research: Planets*, *126*, e2021JE006838. https://doi.org/10.1029/2021JE006838

Lemoine, F. G., Smith, D. E., Rowlands, D. D., Zuber, M. T., Neumann, G. A., Chinn, D. S., & Pavlis, D. E. (2001). An improved solution of the gravity field of Mars (GMM-2B) from Mars Global Surveyor. *Journal of Geophysical Research*, *106*(E10), 23359–23376. https://doi.org/10.1029/2000JE001426

Lewis, S. R., Read, P. L., Conrath, B. J., Pearl, J. C., & Smith, M. D. (2007). Assimilation of thermal emission spectrometer atmospheric data during the Mars Global Surveyor aerobraking period. *Icarus*, *192*(2), 327–347. https://doi.org/10.1016/j.icarus.2007.08.009

Liuzzi, G., Villanueva, G. L., Crismani, M. M. J., Smith, M. D., Mumma, M. J., Daerden, F., et al. (2020). Strong variability of Martian water ice clouds during dust storms revealed from ExoMars Trace Gas Orbiter/NOMAD. *Journal of Geophysical Research: Planets*, *124*. https://doi.org/10.1029/2019JE006250

Malicet, J., Daumont, D., Charbonnier, J., Parisse, C., Chakir, A., & Brion, J. (1995). Ozone UV spectroscopy. II. Absorption cross-sections and temperature dependence. *Journal of Atmospheric Chemistry*, *21*, 263–273. https://doi.org/10.1007/bf00696758

Maltagliati, L., Montmessin, F., Korablev, O., Fedorova, A., Forget, F., Määttänen, A., et al. (2013). Annual survey of water vapor vertical distribution and water-aerosol coupling in the Martian atmosphere observed by SPICAM/MEx solar occultations. *Icarus*, *223*, 942–962. https://doi.org/10.1016/j.icarus.2012.12.012

McElroy, M. B., & Donahue, T. M. (1972). Stability of the Martian atmosphere. *Science*, *177*(4053), 986–988. https://doi.org/10.1126/science.177.4053.986

Montabone, L., Lewis, S. R., Read, P. L., & Hinson, D. P. (2006). Validation of Martian meteorological data assimilation for MGS/TES using radio occultation measurements. *Icarus*, *185*, 113–132. https://doi.org/10.1016/j.icarus.2006.07.012

Montabone, L., Marsh, K., Lewis, S. R., Read, P. L., Smith, M. D., Holmes, J., et al. (2014). The Mars analysis correction data assimilation (MACDA) data set V1.0. *Geoscience Data Journal*, *1*(2), 129–139. https://doi.org/10.1002/gdj3.13

Montabone, L., Spiga, A., Kass, D. M., Kleinböhl, A., Forget, F., & Millour, E. (2020). Martian year 34 column dust climatology from Mars climate sounder observations: Reconstructed maps and model simulations. *Journal of Geophysical Research: Planets*. https://doi.org/10.1029/2019je006111

Montmessin, F., Forget, F., Rannou, P., Cabane, M., & Haberle, R. M. (2004). Origin and role of water ice clouds in the Martian water cycle as inferred from a general circulation model. *Journal of Geophysical Research*, *109*, E10004. https://doi.org/10.1029/2004je002284

Montmessin, F., & Lefèvre, F. (2013). Transport-driven formation of a polar ozone layer on Mars. *Nature Geoscience*, *6*, 930–933. https://doi.org/10.1038/ngeo1957

Nair, H., Allen, M., Anbar, A. D., Yung, Y. L., & Clancy, R. (1994). A photochemical model of the Martian atmosphere. *Icarus*, *111*(1), 124–150. https://doi.org/10.1006/icar.1994.1137

Navarro, T., Madeleine, J.-B., Forget, F., Spiga, A., Millour, E., Montmessin, F., & Määttänen, A. (2014). Global climate modeling of the Martian water cycle with improved microphysics and radiatively active water ice clouds. *The Journal of Geophysical Research: Planets*, *119*, 1479–1495. https://doi.org/10.1002/2013je004550

Neary, L., Daerden, F., Aoki, S., Whiteway, J., Clancy, R. T., Smith, M., et al. (2020). Explanation for the increase in high-altitude water on Mars observed by NOMAD during the 2018 global dust storm. *Geophysical Research Letters*, *47*(7), 1–9. https://doi.org/10.1029/2019gl084354

Newman, C. E., Lewis, S. R., Read, P. L., & Forget, F. (2002). Modeling the Martian dust cycle, 1. Representations of dust transport processes. *Journal of Geophysical Research*, *107*, 5123. https://doi.org/10.1029/2002je001910

Olsen, K. S., Lefèvre, F., Montmessin, F., Trokhimovskiy, A., Baggio, L., Fedorova, A., et al. (2020). First detection of ozone in the mid-infrared at Mars: Implications for methane detection. *Astronomy & Astrophyiscs*, *639*, A141. https://doi.org/10.1051/0004-6361/202038125

Pankine, A., & Tamppari, L. K. (2019). MGS TES observations of the water vapor in the Martian southern polar atmosphere during spring and summer. *Icarus*, *331*, 26–48. https://doi.org/10.1016/j.icarus.2019.05.010

Parkinson, T. D., & Hunten, D. M. (1972). Spectroscopy and Aeronomy of O_2 on Mars. *Journal of Atmospheric Sciences*, *29*, 1380–1390. https://doi.org/10.1175/1520-0469(1972)029<1380:saaooo>2.0.co;2

Patel, M. R. (2021) Data set in support of paper *"ExoMars TGO/NOMAD-UVIS profiles of ozone in Mars Years 34–35: Part 1—Vertical distribution and comparison to water"* [Data set] Open Research Data Online (ORDO) repository. https://doi.org/10.21954/ou.rd.13580336

Patel, M. R., Antoine, P., Mason, J. P., Leese, M. R., Hathi, B., Stevens, A. H., et al. (2017). NOMAD spectrometer on the ExoMars Trace Gas Orbiter mission: Part 2—Design, manufacturing, and testing of the ultraviolet and visible channel. *Applied Optics*, *56*(10), 2771–2782. https://doi.org/10.1364/ao.56.002771

Perrier, S., Bertaux, J. L., Lefèvre, F., Lebonnois, S., Korablev, O., Fedorova, A., & Montmessin, F. (2006). Global distribution of total ozone on Mars from SPICAM/MEX UV measurements. *Journal of Geophysical Research*, *111*(E9). https://doi.org/10.1029/2006je002681

Piccialli, A., Vandaele, A. C., Trompet, L., Neary, L., Viscardy, S., Erwin, J. T., et al. (2021). Impact of gradients at the Martian terminator on the retrieval of ozone from SPICAM/MEX. *Icarus*, *353*, 113598. https://doi.org/10.1016/j.icarus.2019.113598

Quémerais, E., Bertaux, J.-L., Korablev, O., Dimarellis, E., Cot, C., Sandel, B. R., & Fussen, D. (2006). Stellar occultations observed by SPICAM on Mars Express. *Journal of Geophysical Research*, *111*, E09S04. https://doi.org/10.1029/2005JE002604

Rodgers, C. D. (2000). *Inverse methods for atmospheric sounding* (p. 238)Hackensack, N.J: World Sci..

Shimazaki, T., & Shimizu, M. (1979). The seasonal variation of ozone density in the Martian atmosphere. *Journal of Geophysical Research: Space Physics*, *84*(A4), 1269–1276. https://doi.org/10.1029/ja084ia04p01269

Smith, M. D. (2004). Interannual variability in TES atmospheric observations of Mars during 1999–2003. *Icarus*, *167*, 148–165. https://doi.org/10.1016/j.icarus.2003.09.010

Smith, M. D. (2019). THEMIS observations of the 2018 Mars global dust storm. *Journal of Geophysical Research: Planets*, *124*, 2929–2944. https://doi.org/10.1029/2019JE006107

Smith, M. D., Wolff, M. J., Clancy, R. T., & Murchie, S. L. (2009). CRISM observations of water vapor and carbon monoxide. *Journal of Geophysical Research*, *114*(E9). https://doi.org/10.1029/2008JE003288

Snow, M., Machol, J., Viereck, R., Woods, T., Weber, M., Woodraska, D., & Elliott, J. (2019). A revised Magnesium II core-to-wing ratio from SORCE SOLSTICE. *Earth and Space Science*, *6*, 2106–2114. https://doi.org/10.1029/2019EA000652

Steel, L. J., Lewis, S. R., Patel, M. R., Montmessin, F., Forget, F., & Smith, M. D. (2014). The seasonal cycle of water vapor on Mars from assimilation of thermal emission spectrometer data. *Icarus*, *237*, 91–115. https://doi.org/10.1016/j.icarus.2014.04.017

Streeter, P. M., Lewis, S. R., Patel, M. R., Holmes, J. A., & Kass, D. M. (2020). Surface warming during the 2018/Mars Year 34 global dust storm. *Geophysical Research Letters*, *47*(9), e2019GL083936. https://doi.org/10.1029/2019gl083936

Trompet, L., Mahieux, A., Ristic, B., Robert, S., Wilquet, V., Thomas, I. R., et al. (2016). Improved algorithm for the transmittance estimation of spectra obtained with SOIR/Venus Express. *Applied Optics*, *55*(32), 9275. https://doi.org/10.1364/AO.55.009275

Vandaele, A. C., Korablev, O., Daerden, F., Aoki, S., Thomas, I. R., Altieri, F., et al. (2019). Martian dust storm impact on atmospheric H_2O and D/H observed by ExoMars Trace Gas Orbiter. *Nature*, *568*, 521–525.

Vandaele, A. C., Lopez-Moreno, J. -J., Patel, M. R., Bellucci, G., Daerden, F., Ristic, B., et al.. (2018). NOMAD, an integrated suite of three spectrometers for the ExoMars Trace Gas Mission: Technical description, science objectives, and expected performance. *Space Science Reviews*, *214*(5). https://doi.org/10.1007/s11214-018-0517-2

Vandaele, A. C., Neefs, E., Drummond, R., Thomas, I. R., Daerden, F., Lopez-Moreno, J.-J., et al. (2015). Science objectives and performances of NOMAD, a spectrometer suite for the ExoMars TGO mission. *Planetary and Space Science*, *119*, 233–249. https://doi.org/10.1016/j.pss.2015.10.003